Jana Cebulla

MULTI-MODAL IMAGING OF TUMOR VASCULATURE AND TREATMENT RESPONSE IN PRECLINICAL CANCER MODELS

Thesis for the degree of Philosophiae Doctor

Trondheim, June 2015

Norwegian University of Science and Technology
Faculty of Medicine
Department of Circulation and Medical Imaging

NTNU – Trondheim
Norwegian University of
Science and Technology

NTNU
Norwegian University of Science and Technology

Thesis for the degree of Philosophiae Doctor

Faculty of Medicine
Department of Circulation and Medical Imaging

ISBN 978-82-326-1004-4 (printed ver.)
ISBN 978-82-326-1005-1 (electronic ver.)
ISSN 1503-8181

Doctoral theses at NTNU, 2015:174

Printed by NTNU Grafisk senter

Sammendrag

Multimodal avbildning av tumorvaskulatur og behandlingsrespons i prekliniske modeller av kreft

Kreft, en sykdom forårsaket av ukontrollert celledeling, forårsaker betydelig sykelighet og dødelighet i alle folkegrupper. Noen kreftpasienter har meget god prognose etter behandling med kirurgi, stråleterapi eller kjemoterapi, som utgjør bærebjelkene i dagens kreftbehandling. For andre pasienter er det dessverre vanskelig å oppnå et godt behandlingsresultat. Dette skyldes ulike faktorer som dårlige diagnostiske verktøy, inoperabilitet på grunn av tumorens størrelse og lokalisering, metastaserende kreftceller, behandlingsresistens eller dosebegrensende bivirkninger. Det er derfor et stort behov for nye behandlingstilbud for kreftpasienter.

Mange nye legemidler rettet mot deregulerte signalveier i kreftceller er under klinisk utprøvning, og det blir ofte hevdet at denne typen legemidler kan bidra til effektiv, persontilpasset kreftbehandling. For å oppnå dette, trengs det nye metoder for å identifisere hvilke pasienter som vil ha utbytte av de ulike legemidler. Bedre metoder for å predikere behandlingsrespons krever at det utvikles og valideres biomarkører som kan brukes til å monitorere kreftutvikling og behandlingsrespons. Medisinsk avbildning kan potensielt brukes til å identifisere både responderende og behandlingsresistente pasienter tidlig i behandlingen, og dermed hjelpe til å skreddersy behandlingsopplegg for den enkelte kreftpasient. For å oppnå dette trengs det mer kunnskap om hvordan disse nye legemidlene påvirker fysiologiske egenskaper i tumorer.

Angiogenese – dannelse av nye blodkar – er essensielt for tumorvekst og progresjon. Hemming av angiogenesen er derfor ansett som et attraktivt prinsipp for behandling av kreft. I tillegg har det vist seg at legemidler som hemmer signaloverføring i kreftceller, og dermed begrenser celledeling og tumorvekst, kan påvirke blodårenes funksjon. Økt forståelse av angiogenesen og hvordan nye legemidler kan påvirke vaskulær funksjon i tumorer kan derfor bidra til å øke behandlingseffekten i persontilpasset kreftbehandling.

Hovedmålet i dette doktorgradsarbeidet var å evaluere hvordan ulike avbildnings-modaliteter kan brukes til å vurdere morfologi og funksjon av blodkar i tumorer, og å

karakterisere cellulær og vaskulær respons på behandling med et legemiddel som hemmer kreftcellers signalveier. Avhandlingen består av tre artikler, hvor multimodal avbildning ble brukt i studier i xenograft-tumorer i mus.

I den første artikkelen ble mikro-CT, mikro-MRI og *in vivo* MRI brukt til å studere vaskulatur i tumorer med ulik romlig oppløsning. Dette gjorde det mulig å sammenligne ulike teknikker for å estimere blodvolum i tumorer, og dermed bekrefte nøyaktigheten av blodvolumestimater basert på *in vivo* MRI. I den andre artikkelen ble effekten av PI3K-hemmeren BEZ235 evaluert i to forskjellige xenograft-modeller av eggstokkreft ved hjelp av *in vivo* MRI, mikro-CT og histopatologiske metoder. Vi fant at en krefttype med høy aktivitet i PI3K-signalveien responderte godt på behandlingen mens en krefttype med lav aktivitet responderte dårlig. I tillegg fant vi at MRI-markører for celletetthet og histopatologiske markører for proliferasjon hadde bedre prediktive egenskaper enn MRI- og CT-baserte markører for vaskulære endringer. I den tredje artikkelen kombinerte vi dynamisk *in vivo* MRI og intravital mikroskopi for å kunne studere opptaket av nanopartikler i xenograftede eggstokkreft-tumorer. Her fant vi at denne fremgangsmåten var godt egnet til å studere dynamikken i nanopartikkel-opptaket i tumorene *in vivo*, noe som kan være av betydning i forståelsen av hvordan nanopartikler kan brukes til målrettet levering av legemidler til en tumor.

Samlet utgjør disse tre artiklene en helhet, der en rekke forskjellige bruksområder for multimodal avbildning i prekliniske kreftmodeller blir presentert og evaluert. Resultatene i avhandlingen bidrar til utvikling innenfor preklinisk kreftforskning gjennom økt forståelse av hvordan medisinske avbildningsteknikker gjenspeiler fysiologiske forhold i tumorer. Funnene i avhandlingen kan også bidra til mer rasjonell bruk av MR-avbildning i klinisk, persontilpasset kreftbehandling.

Kandidat: Jana Cebulla

Institutt: Institutt for sirkulasjon og bildediagnostikk

Veiledere: Siver A. Moestue, Else Marie Huuse, Tone F. Bathen

Finansiering: The strategic research area medical technology – NTNU

Ovennevnte avhandling er funnet verdig til å forsvares offentlig

for graden Philosophiae Doctor i medisinsk teknologi.

Disputas finner sted i Auditoriet MTA, Medisinsk teknisk forskningssenter

Fredag 19. juni 2015, kl. 12.15.

Acknowledgement

The work presented in this thesis has been carried out in the MR Cancer group, Department of Circulation and Medical Imaging, NTNU. The work was funded by "The strategic research area medical technology" of NTNU.

I would like to thank everyone who has supported me and has contributed to the completion of this thesis.

First and foremost, I would like to express my gratitude to my supervisors Dr. Siver A. Moestue, Dr. Else Marie Huuse and Prof. Tone F. Bathen. Thank you for always being available for discussions, commenting on my writing and encouraging feedback. Siver, thank you for your quick responses whenever I needed your guidance. Else Marie, thank you for your help with setting up MRI protocols, experiments and data analysis. And Tone, thank you for creating such a nice working environment. Several other people played central roles in the work I perfomed in the recent years. Prof. Ingrid Gribbestad was supervising the initial stages of my PhD and made me feel very welcome in the MR cancer group, for which I am very grateful. My sincere thanks also go to Prof. Arvind Pathak for welcoming me several times in your lab, introducing me to preclinical cancer research and teaching me valuable skills. My thanks also go to Dr. Sjoerd Hak, I appreciate that you let me take part in your nanoparticle study and especially for teaching me how to cannulated tail veins and coming to the lab in the evening or weekend, when I was not mastering this technique yet.

I also wish to thank all co-authors and the numerous people who have contributed to my papers. Thanks to Prof. Geir Bjørkøy for the contributions on characterizing the ovarian cancer cells used in several of my studies, Dr. Sonja Andersen, Kristine Pettersen and Anna van der Veen for providing ovarian cancer cells for several studies and performing *in vitro* work and Prof. Wenche Prestvik for her help with p-Akt quantifications. Also Prof. Anna Bofin deserves my sincere thanks for her help with interpreting histological images.

Further, I would like to thank everyone else who has provided technical assistance. From the MR environment I would like to thank Øystein Risa, Tina B. Pedersen and

Marius Widerøe for their assistance with technical problems. I would also like to thank the Cellular and Molecular Imaging Core Facility at NTNU for their assistance with pathology and microscopy and the Animal Facility at NTNU for their assistance with animals.

I would like to thank the people working at the Radiology Department of The Johns Hopkins University School of Medicine, for providing a good working environment during my stay in Baltimore and especially Prof. Jiangyang Zhang for help with establishing the MRI protocols.

My thanks also go to all colleagues at the MR center for creating a friendly working atmosphere and being friends at the same time as colleagues.

Moreover, I would like to thank my family and friends for their constant support: Vielen Dank an meine Eltern für eure stetige Unterstützung während meiner gesamten Ausbildung. Danke, dass ihr immer ein offenes Ohr für mich habt. Ich danke auch meiner restlichen Familie für eure Ermutigungen. Danke Opa, dass du immer sagst „Du schaffst das schon“. Auch wenn ich es leider immer verneinen muss, wenn ihr mich fragt, ob ich schon ein Mittel gefunden habe um Krebs zu heilen - ich hoffe, dass meine Arbeit die Forschung ein Stück weiter bringt.

Finally, thank you, Eugene, for always supporting and encouraging me throughout this process and being there for me to discuss our work, but also for making my life outside of work interesting.

Jana Cebulla

Trondheim, March 2015

Summary

Multi-modal imaging of tumor vasculature and treatment response in preclinical cancer models

Cancer, a disease characterized by uncontrolled cell growth, causes significant morbidity and mortality across the world. Some cancers can successfully be treated with the standard therapies – surgery, radiotherapy or chemotherapy. However, many types of cancer are challenging to treat because of various factors such as poor diagnostic procedures, inoperability due to tumor location, formation of metastases, treatment resistance, and dose-limiting side effects of therapies. Therefore, improved treatment strategies are urgently needed.

New drugs targeting the dysregulated signaling pathways in cancer are being tested in clinical trials, and it is frequently suggested that these drugs can contribute to personalized treatment of cancer. To achieve this, novel methods for identifying the right drugs for the right patients are required. Improved prediction of treatment response requires development and validation of biomarkers that can monitor cancer development and treatment response. Using medical imaging to identify treatment responders or non-responders at early time points can therefore contribute to improved tailoring of therapy to individual cancer patients. To achieve this, we need to understand how these targeted drugs affect tumor physiology.

Angiogenesis, the formation of new blood vessels, which is essential for tumor growth and progression, is an attractive therapeutic target. Furthermore, drugs targeting signaling pathways that drive cellular proliferation have also been reported to interfere with the vascular function in tumors. A better understanding of angiogenic processes and vascular changes resulting from targeted cancer treatment is therefore needed.

The main objective of this thesis was to evaluate different imaging modalities in their ability to assess tumor vascular morphology and function, and to characterize cellular and vascular response to targeted treatment. The thesis consists of three papers, in which multi-modal imaging was performed on cancer xenografts grown in mice.

In the first paper, high resolution micro-CT, micro-MRI and *in vivo* MRI were combined to examine the vasculature of breast tumor xenografts at multiple spatial scales. The use of multi-modal imaging allowed the validation of *in vivo* MRI biomarkers of blood volume.

In the second paper, tumor response to BEZ235, a drug inhibiting the PI3-kinase pathway, was studied in two ovarian xenograft types with *in vivo* MRI, micro-CT and histology. We found that the xenograft type with upregulated PI3-kinase activity responded strongly to the treatment while the type with lower PI3-kinase activity did not. In addition, we found that MRI biomarkers of cell density and histological markers of cell proliferation were better indicators for response to this treatment than MRI and CT biomarkers of vascular change.

In the third paper, we combined dynamic *in vivo* MRI and intravital microscopy to quantify uptake of nanoparticles in ovarian tumor xenografts. It was found that this approach may be well suited to study nanoparticle dynamics on the whole tumor level *in vivo*, which is of importance e.g. for the use of nanoparticles as drug carriers.

Collectively, this thesis presents a wide spectrum of possible applications of multi-modal imaging for preclinical cancer research. Also, the potential utility of *in vivo* MRI biomarkers in clinical cancer imaging is discussed. The results of this thesis therefore contribute to advancing preclinical cancer research, but also to clinical implementation of multimodal MR imaging in cancer.

Symbols and abbreviations

$\|\alpha>$	low energy spin state
$\alpha_v\beta_3$	Alpha-v beta-3 integrin
$\|\beta>$	high energy spin state
^1H	hydrogen
ADC	apparent diffusion coefficient
AIF	arterial input function
Akt	Protein kinase B
B_0	external magnetic field strength
B_1	temporarily applied magnetic field strength
C	contrast agent concentration
CT	computed tomography
δ	diffusion gradient duration
Δ	time between two diffusion gradients
ΔE	energy difference
$\Delta\chi$	susceptibility difference between blood with and without contrast agent
DAPI	4',6-diamidino-2-phenylindole
DCE	dynamic contrast enhanced
DW	diffusion weighted
E	energy
EES	extracellular, extravascular space
Ef	extraction fraction
EPR	enhanced permeability and retention
F	blood flow per unit mass of tissue
G	gradient strength
γ	gyromagnetic ratio
Gd	Gadolinium
Gd-DTPA	Gadopentetic acid
$\hbar$	reduced Plack constant
Hct	blood hematocrit
HES	hematoxylin, eosin, saffron
HIF-1α	hypoxia-inducible factor 1
HUVEC	human umbilical vein endothelial cells
I	X-ray intensity
i.v.	intraveneous

IVM	intravital microscopy
k	Boltzmann constant
k_{ep}	rate constant between EES and blood plasma
K_i	transfer constant from plasma to EES
K^{trans}	volume transfer constant between blood plasma and EES
M	magnetization
MRI	magnetic resonance imaging
mTORC1	mammalian target of ramapycin complex 1
mTORC2	mammalian target of ramapycin complex 2
μ	magnetic moment (chapter 1.2)
	X-ray attenuation coefficient (chapter 1.3)
μCT	micro-computed tomography
μMRI	magnetic resonance microscopy
N	population of spin states
NMR	nuclear magnetic resonance
NO	nitric oxide
NOS	nitric oxide synthase
ω_0	Larmor frequency
p-	phosphorylated
PDK1	3-phosphoinositide dependent kinase-1
PET	positron emission tomography
PI3K	phosphatidylinositol 3-kinase
PIK3CA	phosphatidylinositol-4,5-bisphosphate 3-kinase, catalytic subunit alpha
PIP_2	phosphatidylinositol-4,5-bisphosphate
PIP_3	phosphatidyl-inositol-3,4,5-triphosphate
PSA	prostate specific antigen
PTEN	phosphatase and tensin homolog
R_1	longitudinal relaxation rate
R_2	transverse relaxation rate
$r_{1,2}$	relaxivity
RARE	rapid acquisition with refocused echoes
RECIST	Response Evaluation Criteria in Solid Tumors
rf	radio frequency
RGD	Arginylglycylaspartic acid (Arg-Gly-Asp)
ρ_p	proton density
ρ_t	tissue density

RTK	receptor tyrosine kinase
S	signal intensity
SCID	severe combined immunodeficiency
SPECT	single photon emission computed tomography
SSC	steady state susceptibility contrast
STI	signal transduction inhibitor
T	temperature
T_1	longitudinal relaxation time
T_2	transverse relaxation time
TE	echo time
TR	repetition time
v_e	volume of EES per unit volume of tissue
VEGF	vascular endothelial growth factor
VIF	vascular input function
v_p	blood plasma volume per unit volume of tissue

List of papers

Paper I

Multiscale and multi-modality visualization of angiogenesis in a human breast cancer model

Jana Cebulla, Eugene Kim, Kevin Rhie, Jiangyang Zhang, Arvind P. Pathak

Angiogenesis. 2014 Jul;17(3):695-709.

Paper II

MRI Reveals the in Vivo Cellular and Vascular Response to BEZ235 in Ovarian Cancer Xenografts with Different PI3-Kinase Pathway Activity

Jana Cebulla, Else Marie Huuse, Kristine Pettersen, Anna van der Veen, Eugene Kim, Sonja Andersen, Wenche S. Prestvik, Anna M. Bofin, Arvind P. Pathak, Geir Bjørkøy, Tone F. Bathen, Siver A. Moestue

Br J Cancer 2015 Feb 3;112(3):504-13.

Paper III

Periodicity in tumor vasculature targeting kinetics of ligand-functionalized nanoparticles studied by dynamic contrast enhanced magnetic resonance imaging and intravital microscopy

Sjoerd Hak, Jana Cebulla, Else Marie Huuse, Catharina de L. Davies, Willem J.M. Mulder, Henrik B.W. Larsson, Olav Haraldseth

Angiogenesis. 2014 Jan;17(1):93-107.

Contents

1 Introduction **1**
1.1 Cancer ... 1
1.1.1 Breast Cancer ... 1
1.1.2 Ovarian Cancer ... 2
1.1.3 Targeted cancer treatment ... 2
1.1.4 Tumor vasculature and angiogenesis ... 3
1.1.5 Anti-angiogenic therapy ... 4
1.1.6 $\alpha_v\beta_3$ integrin ... 5
1.1.7 PI3K pathway in cancer ... 6
1.1.8 Biomarkers for therapy stratification and treatment response ... 8
1.1.9 Tumor microenvironment ... 8
1.1.10 Animal models of cancer ... 9
1.1.11 Medical imaging in cancer ... 10
1.2. Magnetic resonance imaging ... 11
1.2.1 Basics of nuclear magnetic resonance ... 11
1.2.2 Relaxation ... 13
1.2.3 MRI contrast agents ... 15
1.2.4 Spatial encoding ... 15
1.2.5 MRI pulse sequences ... 16
1.2.6 Diffusion weighted MRI ... 18
1.2.7 Dynamic contrast-enhanced MRI ... 20
1.2.8 Steady state susceptibility contrast MRI ... 24
1.3 X-ray computed tomography ... 25
1.4 Histopathology ... 27
1.5 Intravital microscopy ... 27
1.6 Multifunctional nanoparticles ... 28

2 Aims **31**

3 Materials and methods **33**
3.1 Cell lines and animal models ... 33
3.1.1 MDA-MB-231 human breast cancer cell line ... 34
3.1.2 TOV-21G and TOV112D human ovarian cancer cell lines ... 34
3.2 Drug BEZ235 ... 34
3.3 *In vivo* MRI ... 35
3.4 μCT ... 35
3.5 Oil-in-water nanoemulsions ... 35
3.6 Intravital microscopy ... 37

3.7 Histopathology 37
3.8 Protein Expression 37

4 Summary of papers **39**
Paper I 39
Paper II 40
Paper III 41

5 Discussion **43**
5.1 Multi-modal imaging for validating imaging biomarkers 43
5.1.1 Validating SSC-MRI-derived tumor FBV using μCT 44
5.1.2 Validating changes in ADC as a biomarker for cellular response using histology 45
5.1.3 Validating *in vivo* cell targeting kinetics by *in vitro* cell targeting experiments 45
5.2 Multi-modal imaging of tumor vessel morphology and function 47
5.2.1 Imaging of vascular morphology 49
5.2.2 Imaging of *in vivo* nanoparticle distribution in tumors using DCE-MRI and IVM 50
5.2.3 Imaging of vascular function 52
5.3 Multimodal imaging of drug response 53
5.3.1 Cellular response to PI3K/mTor inhibition 53
5.3.2 Imaging of changes in vascular function and morphology induced by PI3K inhibition 54
5.3.3 Cellular versus vascular response 56

6 Conclusions and future perspectives **59**

7 Bibliography **61**

1 Introduction

1.1 Cancer

Cancer is a large group of complex and heterogeneous diseases, characterized by uncontrolled cell division and the potential to invade other tissues and spread to distant sites, a process called metastasis [1,2]. There exist more than 100 types of cancer [2,3], but there are certain characteristics that are thought to be acquired by all cancer cells to empower their survival, proliferation and spread [4]. In 2000, Hanahan and Weinberg termed these traits the "hallmarks of cancer" and listed them as "sustaining proliferative signaling", "evading growth suppressors", "activating invasion and metastasis", "enabling replicative immortality", "inducing angiogenesis" and "resisting cell death" [3]. About 10 years later, this list was revised and "deregulating cellular energetics" and "avoiding immune destruction" were added as "emerging hallmarks" [4]. In addition, two "enabling characteristics" – "genome instability and mutation" and "tumor promoting inflammation" – were discussed [4].

Its complexity and heterogeneity make cancer difficult to treat. Cancer is one of the leading causes of death with 8.2 million cancer deaths and 14.1 million new cancer cases in 2012 worldwide [5]. While the age-standardized incidence rate of cancer has mostly been stable or rising, the mortality rates have been decreasing over the past 20 years [5], which may be attributed to the improved cancer detection and treatment options available to us today. Best treatment outcome is achieved when the cancer is detected early, before it has metastasized. The current treatment options are surgery, radiotherapy, chemotherapy and new targeted therapies.

1.1.1 Breast Cancer

Breast cancer is the most frequent type of cancer diagnosed in women and is the second leading cause of cancer mortality in women in developed countries after lung cancer [5]. Most breast cancer patients receive breast conserving surgery or mastectomy, often with adjuvant radio- or chemotherapy and, in some cases, supported by targeted therapies [6]. Especially patients with late-stage breast cancer receive chemotherapy with or without other therapies [6]. In Norway and the USA, the overall 5-year survival rate is

about 89%, which is relatively high, but for patients with distant metastases (about 5%), the 5-year survival rate is dramatically reduced to about 26% [7,8]. In addition, the most aggressive breast cancer types are often found in women below 50 [8]. The high incidence of breast cancer and the high mortality rates of mostly younger women with aggressive subtypes of the disease have propelled large investments in breast cancer research.

1.1.2 Ovarian Cancer

Ovarian cancer is the most lethal form of gynecological cancer because most cases are diagnosed when the cancer has already metastasized. The overall five-year survival rate is only about 45% [8,9]. The standard treatment for ovarian cancer is cytoreductive surgery and platinum-based chemotherapy combined with taxane or, more recently, liposomal doxorubicin [10]. Most patients respond well to first-line therapy; however, the median progression-free survival is only 18 months [11], and the patients often relapse with chemotherapy-resistant cancer [10]. For over 30 years, the treatment has not changed much [10] and accordingly, the 5-year survival rates have only slightly increased [8,10]. Hence, new therapeutic approaches such as targeted therapies are urgently needed to improve patient survival [10,12].

1.1.3 Targeted cancer treatment

While conventional chemotherapy is cytotoxic to all rapidly diving cells, targeted therapies are more specifically directed at cancer cells by interfering with molecules directly linked to the cancer cells' proliferation and survival with less side effects on healthy tissue [13]. Targeted cancer therapies are a form of precision medicine, where the patient's genetic or protein expression profile is analyzed for abnormal activity to identify potential therapeutic targets and to develop a treatment plan. Targeted therapies include hormone therapy, signal transduction inhibitors (STIs), angiogenesis inhibitors and others [13].

Although research has provided remarkable advances in knowledge about the hallmarks of cancer and the biological mechanisms that cancer cells utilize in their favor, the large

network of interacting pathways is so complex that we still cannot reliably predict if a cancer will respond to treatment. In addition, cancers often develop resistance to targeted treatments through mutation or circumvention of a specific pathway by relying on other pathways instead [4,13]. These adaptive mechanisms are not yet understood sufficiently, and unfortunately, resistance often limits long-term disease control.

1.1.4 Tumor vasculature and angiogenesis

Angiogenesis is the formation of blood vessels from pre-existing vasculature. It is required for cancers to grow beyond a size of about 2-3 mm and satisfy their need for oxygen and nutrients [14]. Angiogenesis is listed as one on the hallmarks of cancer [3] as it is essential for cancer growth, invasion and metastasis [15].

Pro- and anti-angiogenic molecules regulate the growth of new blood vessels and are usually balanced in normal tissue. Certain triggers, however, can disturb this balance in the favor of pro-angiogenic molecules. These can be produced e.g. by cancer cells, endothelial cells or fibroblasts. Perhaps the best characterized trigger for the production of pro-angiogenic molecules is hypoxia, but also other factors like pH, mechanical stress, inflammatory response and genetic alterations can influence their production [16]. Hypoxia arises when the nearest functional blood vessel is too far away to deliver sufficient oxygen to the tumor cells [16]. A low intracellular oxygen concentration induces the expression and activation of the α subunit of hypoxia-inducible factor 1 (HIF-1α) [17]. This, in turn, leads to the production of vascular endothelial growth factor (VEGF), which, among other factors, promotes the growth of new blood vessels [17,18].

The overproduction of pro-angiogenic factors causes the tumor vasculature to be abnormal both in morphology and function [19]. Compared to normal blood vessels, tumor vessels are disorganized, tortuous, often dilated, with numerous branches, arteriovenous shunts or blind ends [16] (**Fig. 1**). Some areas in a tumor can be highly vascularized while other areas contain only few vessels [19]. In addition, tumor vasculature is hyperpermeable to macromolecules [20], which causes high interstitial

fluid pressure [19]. These traits lead to a poorly functioning tumor vasculature with turbulent blood flow and poor perfusion, which may lead to vessel collapse [19].

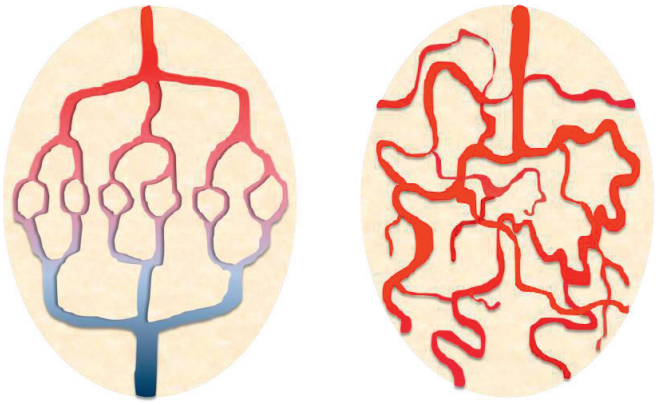

Figure 1: Normal blood vessels (left) versus tumor blood vessels (right). Normal vessels form highly organized capillary beds which are well suited for the delivery of oxygen and nutrients to the tissue. Tumor vessels are disorganized with large, tortuous vessels, blind ends and frequent branching, which may lead to poor perfusion and collapse of non-functional vessels.

These vascular abnormalities do not seem to be a disadvantage for the tumor but may even contribute to greater malignancy. Vascular function is also of great importance for traditional cancer therapy [19]. Dysfunctional vasculature makes the delivery of chemotherapeutics to the tumor challenging and low oxygen levels can reduce the efficacy of radiation therapy [19].

1.1.5 Anti-angiogenic therapy

In 1971, Judah Folkman was the first to suggest "anti-angiogenic" therapy as a new mode of cancer treatment. Today, there are several clinically approved drugs that directly or indirectly target angiogenesis, and many more are in development. The first and most widely used VEGF inhibitor is bevacizumab, which today is approved for the treatment of several types of cancer [21], e.g. in combination with chemotherapy for metastatic colorectal cancer, renal cancer and platinum resistant and reoccurring epithelial ovarian cancer [22,23]. Despite high expectations for its anti-cancer efficacy, only modest benefits have been demonstrated as many clinical studies fail to report improvements in overall survival [21]. One major problem associated with the limited

effects of anti-angiogenic therapy is an intrinsic or acquired resistance to the drugs, which can be caused e.g. through the activation of alternative signaling pathways [24]. This may even lead to the development of more aggressive cancer with increased metastatic potential [21].

A large number of clinical trials are still being conducted to gather more data on the efficacy of anti-angiogenic agents in various types of cancer, mostly as combination-therapy and also as adjuvant or neoadjuvant therapeutics [21]. However, to tackle the biggest challenge of predicting drug efficacy under various conditions such as cancer type, stage and drug combinations, it will be necessary to conduct more preclinical studies to better understand how these drugs affect the tumors and their vasculature and what factors lead to further tumor progression. Especially the use of more relevant preclinical cancer models will be important [21].

1.1.6 $\alpha_v\beta_3$ integrin

Alpha-v beta-3 ($\alpha_v\beta_3$) integrin expression is upregulated in some cancer cells and is also highly expressed on the surface of tumor endothelial cells, facilitating their migration and thereby influencing tumor angiogenesis [25]. Integrins are a family of transmembrane receptors consisting of one α and one β subunit. They are mediators of cell-cell adhesion and cell adhesion to extracellular matrix proteins [26] and thus play important roles in cell spreading and migration [16]. Integrins can also activate various signaling pathways [26].

Integrin $\alpha_v\beta_3$ belongs to a subgroup of integrins that recognize proteins containing the amino-acid sequence Arg-Gly-Asp (RGD) through which it binds certain extracellular matrix proteins such as fibronectin and vitronectin [26,27]. The expression of $\alpha_v\beta_3$ is stimulated by several angiogenic growth factors and its availability on the cell surface is regulated by a dynamic process of endocytotic recycling, in which the integrin is internalized into the cell via endocytosis and recycled back to the cell surface without degradation [28]. This receptor recycling has been found to happen via two different mechanisms that require about 3 and 10 minutes, respectively, for half of the integrins to perform one recycling loop [28].

The upregulation of $\alpha_v\beta_3$ on angiogenic tumor vasculature has motivated the development of cilengitide, an inhibitor of $\alpha_v\beta_3$ and $\alpha_v\beta_5$, but so far it has not shown substantial clinical anticancer treatment effects [29]. A better understanding of processes involving $\alpha_v\beta_3$ functionality and targeting is therefore necessary. Especially non-invasive preclinical visualization and quantification methods for in vivo integrin expression and dynamics may be essential [30]. For this purpose, various compounds containing the RGD peptide for $\alpha_v\beta_3$ targeting properties have been produced, for example with radioactive properties for PET imaging, fluorescent properties for optical imaging, or paramagnetic properties for magnetic resonance imaging [30].

1.1.7 PI3K pathway in cancer

One signal transduction pathway often upregulated in cancer is the phosphatidylinositol 3-kinase (PI3K) pathway, which is an important regulator of cellular functions such as growth, proliferation, apoptosis and metabolism [31].

PI3Ks are a family of intracellular lipid kinases that phosphorylate the 3´-hydroxyl group of phosphatidylinositol and phosphoinositides (i.e. the phosphorylated forms of phosphatidylinositol). There are three classes of PI3Ks, grouped according to their structure and substrate preference [32]. The class I PI3Ks can be activated by growth factor receptor tyrosine kinases (RTKs) or G-protein-coupled receptors as illustrated in **Fig 2**.

In response to extracellular signals, Class I PI3K primarily catalyzes the phosphorylation of phosphatidylinositol-4,5-bisphosphate (PIP_2) to phosphatidyl-inositol-3,4,5-triphosphate (PIP_3). This process is directly opposed by the phosphatase and tensin homolog (PTEN), which negatively regulates the pathway activity [31]. PIP_3 can recruit and bind the serine-threonin kinase AKT, which can be activated by phosphorylation at threonine 308 by 3-phosphoinositide dependent kinase-1 (PDK1) and at serine 473 by the rapamycin-insensitive mammalian target of ramapycin complex (mTORC2) [31,33]. Phosphorylated AKT (p-AKT) is of central importance for the regulation of numerous biological processes [34]. For instance, p-AKT leads to the activation of the rapamycin-sensitive mTOR complex (mTORC1). This complex

activates p70S6 kinase, which, in turn, phosphorylates S6 ribosomal protein and ultimately increases protein synthesis [35,36].

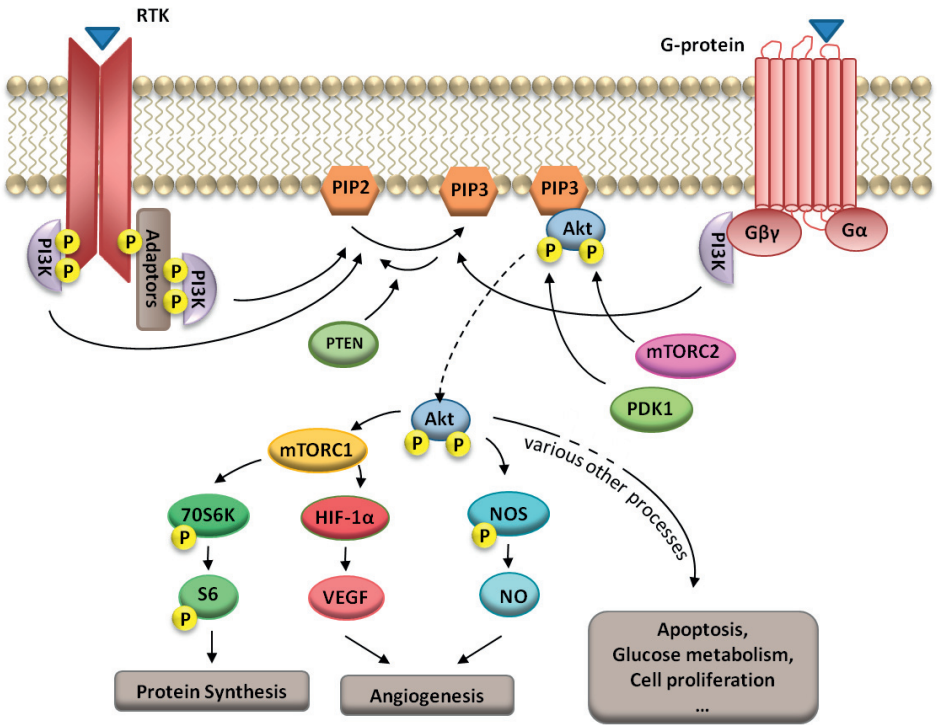

Figure 2: Schematic illustration of the PI3K signaling pathway as explained in the text. Note that this is a simplified and incomplete representation of the pathway. Figure based on [31-39].

Angiogenesis is thought to be mainly induced by hypoxia, but also the PI3K pathway has a role in the regulation of angiogenesis [37]. In recent years it was shown that HIF-1 activity is influenced by PI3K pathway activity in cancer cells, which results in the expression of VEGF [17,37,38]. Furthermore, phosphorylation of AKT can lead to activation of nitric oxide synthase (NOS), which can induce angiogenesis by producing nitric oxide (NO) [39].

Important effectors found to be dysregulated in cancer include phosphatidylinositol-4,5-bisphosphate 3-kinase, catalytic subunit alpha (PIK3CA); PTEN; and Akt [32]. Since the PI3K pathway is so important for cancer development, drugs inhibiting PI3K, Akt or mTOR have been developed and are currently undergoing clinical trials [37,38].

1.1.8 Biomarkers for therapy stratification and treatment response

In cancer patients, a treatment plan is usually established after evaluation of tumor type, location and size, as well as histopathological and molecular analyses. However, it is difficult to reliably predict drug treatment response using genetic information [40]. Furthermore, the development of drug resistance is difficult to predict. Therefore, response is usually evaluated after treatment onset by measuring tumor size according to the RECIST guidelines, which are the 'Response Evaluation Criteria in Solid Tumors' [41]. For some cancers, also blood-based markers can be used for cancer detection and assessment of treatment response. For example, elevated prostate specific antigen (PSA) can indicate prostate cancer [42], while CA 125 is a serum protein often elevated in ovarian cancer patients [43]. Unfortunately, these blood-based biomarkers have limited predictive value [42,44], especially when they are assessed early during treatment [45]. Also tumor volume-based response assessment is not always optimal since volume decrease may occur slowly, and especially for molecularly targeted drugs, response is often associated with functional (e.g. vascular or cytological) rather than volumetric changes [46-48]. This highlights a need for novel non-invasive biomarkers for assessment of early response in order to enable prompt detection of therapeutic resistance and timely adjustment of treatment strategies for non-responders. This is important especially for the patients, as it will minimize unnecessary side effects from ineffective treatment. In addition, better customization of treatment can help to reduce costs for drugs and other healthcare services. Functional imaging biomarkers are now being investigated for early assessment of treatment-induced changes in tumor cellularity, vascularization or metabolic activity [47].

1.1.9 Tumor microenvironment

To understand the complex biology of tumors, one needs to look at tumor cells in their microenvironment, which consists of cells, vasculature and interstitium, also called the extracellular, extravascular space (EES) [49].

The cellular component of tumors is composed of cancer cells, cancer stem cells and non-cancerous cells, among which are immune inflammatory cells, fibroblasts, endothelial cells and pericytes [4]. The latter two make up the blood vessels, which

supply the tumor with oxygen and nutrients. The EES is made up of the extracellular matrix, a hydrophilic gel consisting of interstitial fluid, macromolecules and collagen fibers. The interstitial fluid pressure is characteristically elevated in tumors, increases towards the tumor core, and is higher for large tumors [49].
A complex network of interactions between the cancer cells and their microenvironment is formed as the tumor progresses and is the basis for the development of high-grade malignant tumors with metastatic potential [4].

1.1.10 Animal models of cancer

Cancer cell lines are an important tool for the *in vitro* characterization of gene expression, signaling pathways or metabolism on a cellular level. However, *in vitro* experiments of drug sensitivity have been shown to be strongly dependent on the study design [50]. In addition, the tumor microenvironment plays an important role in cancer development [4]. For instance, while endothelial cells can be grown *in vitro* to study their cellular characteristics, the full complexity of tumor angiogenesis can only be recapitulated *in vivo*, where the entire microenvironment is involved in the induction of blood vessel growth. Therefore, the use of suitable preclinical cancer models is a necessary step for the in-depth characterization of cancer as a biological system, the study of treatment response or resistance, and the establishment of new biomarkers for cancer detection and treatment response. Especially for the development of new drugs, animal testing is required before drugs can be tested in a clinical setting [51].

In preclinical research, tumors either develop spontaneously in transgenic animals, are induced by e.g. carcinogens, or are grown from xenografts of cancer cells or cancer tissue from patients. Xenografts are frequently used for medical imaging studies because they grow relatively quickly and are easy to use [52]. The growth of xenografts grown from human cancer cells or tissue requires immunodeficient mice such as severe combined immunodeficiency (SCID) mice or mice with a Foxn1nu mutation that have an abnormal thymus and lack fur (nude). Tumor xenografts grown from cell lines cannot perfectly model human cancer because of differences in the initiation of the tumor development, metastasis formation and the tumor microenvironment, e.g. due to the lack of immune cells and a homogeneous cancer cell population [53]. In addition,

drug response in clinical trials is often lower than expected from results in tumor xenografts [54]. Nevertheless, subcutaneous xenografts grown from tumor cell lines have provided relevant information to the clinic [55] and many cell lines are very well characterized and commercially available, which can make the comparison of studies using the same cell lines easier. Therefore, xenografts are still frequently used in preclinical research and are helpful tools for developing tumor or vascular imaging methods and biomarkers.

1.1.11 Medical imaging in cancer

Since the introduction of the X-ray, medical imaging has increasingly contributed to the diagnosis and follow-up of cancer patients. Today, medical imaging is increasingly being used in all stages of the disease for prediction, screening, staging, prognosis, therapy planning, response, recurrence and palliation [56]. The imaging modalities available today are based on different physical principles and therefore vary greatly in resolution, contrast and sensitivity. For example, X-ray and computed tomography (CT) rely on the attenuation of X-rays in the body, positron emission tomography (PET) and single photon emission computed tomography (SPECT) detect the distribution of radioactive tracers in the body, magnetic resonance imaging (MRI) uses low frequency microwaves and strong magnetic fields to create images of various contrasts, and ultrasound uses acoustic waves and their reflection to image different tissue structures. The choice of imaging modalities depends on the application, e.g. screening for breast cancer is performed by X-ray mammography (mostly due to lower costs and higher availability), while MRI is better suited for diagnosing and monitoring cancer due to better resolution and various available image contrast techniques. The use of multi-modal imaging in cancer is increasing due to the complementary information available from different imaging techniques and dual imaging systems such as PET/CT or PET/MR have been developed for this purpose.

In the following chapters, the imaging modalities used for this thesis are described in more detail.

1.2. Magnetic resonance imaging

Magnetic resonance imaging (MRI) is based on the principles of nuclear magnetic resonance, which were first described by Rabi in 1938 [57] and for which he earned the Nobel Prize in Physics in 1944. This was followed by another Nobel Prize in 1952 for Bloch and Purcell who measured nuclear magnetic resonance (NMR) signals in water and paraffin [58,59]. But it was not until 1973 that Lauterbur [60] and Mansfield [61] described how NMR can be used to create images for which they were awarded the Nobel Prize in Physiology or Medicine in 2003.

Today, MRI is a well-established medical imaging method that is very versatile as it is sensitive to a wide array of tissue properties and provides unique soft tissue contrast. This makes MRI a powerful technique to study diseases including cancer. Moreover, MRI is non-invasive and does not involve ionizing radiation, which is highly beneficial when a repeated assessment of disease progression and treatment response is required.

The physics behind MRI is rather complex, so here, only certain basic and simplified principles will be discussed. A more comprehensive explanation of NMR can be found in [62] and a description from MRI basics to advanced imaging techniques can be found e.g. in [63].

1.2.1 Basics of nuclear magnetic resonance

NMR is based on the intrinsic property of atomic nuclei to possess a spin, which can be systematically manipulated with external magnetic fields. The nuclear spin depends on the number of protons and neutrons which each have a spin of ½. Depending on their composition, atomic nuclei can have various spin configurations, but for nuclei with an even number of protons and neutrons, the formation of antiparallel spin pairs leads to a net spin of zero. Among these nuclei are carbon-12 (^{12}C) and oxygen-16 (^{16}O), which are highly abundant in biological tissue. Only their rare isotopes ^{13}C and ^{17}O have non-zero spins. Hydrogen-1 (^{1}H), with its core consisting of just a proton, has spin of ½ and makes up about 67% of the atoms in biological tissue, mainly in the form of water. In medical MRI we therefore rely on ^{1}H nuclei (i.e., protons) and their different features such as their density or mobility to gain image contrast.

The spin property of a proton is directly linked to the existence of a magnetic moment μ. When an external magnetic field B_0 is applied (by convention along the z-axis), this magnetic moment precesses around the axis of B_0 at the frequency ω_0, which is called the Larmor frequency and is proportional to the external magnetic field (**Fig. 3A**).

$$\omega_0 = \gamma B_0 \tag{1.1}$$

The constant γ is the gyromagnetic ratio and characteristic for each nucleus. For protons, γ is 42.6MHz/tesla.

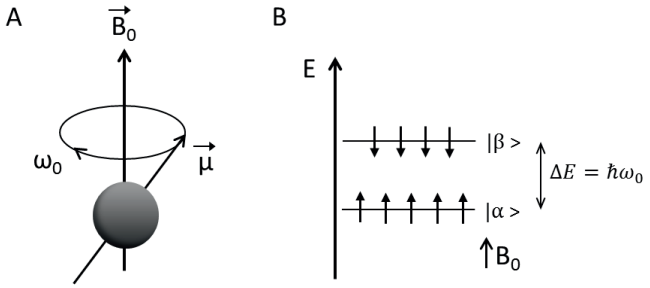

Figure 3: A) A proton possesses a magnetic moment μ, which is the result of its intrinsic property of possessing a spin. An external, static magnetic field B_0 will produce a torque that forces the magnetic moment to precess around the axis of the magnetic field with the frequency ω_0. B) In an external magnetic field B_0, proton spins can have two polarization states, one parallel and one antiparallel to B_0. The energy difference between the two states is directly proportional to the Larmor frequency ω_0 with the reduced Planck constant ħ as the proportionality factor.

In the quantum mechanical description, proton spins can be in two different states |α> and |β>, which are said to be polarized along the positive or negative z-axis, which commonly defines the direction of B_0. These states are usually illustrated by arrows pointing along the positive or negative z-axis (**Fig. 3B**). The parallel state has lower energy than the antiparallel state and the energy difference equals $\hbar\omega_0$ and is proportional to B_0 with equation (1.1). In thermal equilibrium, the high energy state is slightly less populated than the low energy state, which is determined by the Boltzmann distribution.

$$\frac{N_\beta}{N_\alpha} = e^{-\frac{\hbar\boldsymbol{\omega_0}}{kT}} \tag{1.2}$$

where N is the population of the |α> and |β> state, respectively, k is the Boltzmann constant and T the temperature.

In an ensemble of many protons, the sum of magnetic moments of all protons will form a net magnetization M that is pointing along the z-axis, called longitudinal magnetization. This magnetization vector is manipulated and observed in MRI.

By applying a radiofrequency (rf) -pulse with the amplitude B_1, tuned to the resonance frequency ω_0 and perpendicular to B_0, we can tilt the magnetization away from the z-axis (**Fig. 4**).

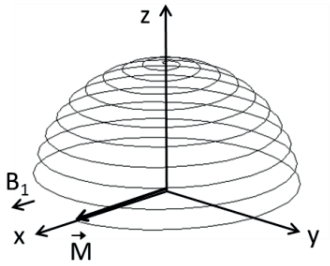

Figure 4: Trajectory of magnetization during the application of a 90° rf-pulse.

This radiofrequency pulse is also called an 'excitation pulse'. The angle by which the magnetization is rotated depends on the magnitude and duration of the pulse. A so called 90°-pulse, rotates M into the transverse plane, i.e. the x-y-plane, where it will precess around the z-axis and induce an electric current in a receiver coil, which is the measured signal in MRI.

1.2.2 Relaxation

T_1 relaxation

After excitation, the magnetization will turn back to its equilibrium state along the B_0 direction as the excited protons release energy to their surroundings. This regain of magnetization is called longitudinal or T_1 relaxation, where T_1 describes the time by which about 63% of the equilibrium magnetization M_0 is reached after a 90°-pulse. The energy loss of protons can only occur if they encounter magnetic fields fluctuating at the

Larmor frequency, which is influenced by the mobility of protons and their surroundings. Thus, different types of tissue have different T1 relaxation times, creating contrast in T_1-weighted MR images.

T_2 relaxation

Another mechanism of loss of the detectable transverse magnetization is spin dephasing. After a 90°-pulse the spins are 'in-phase', but due to local, fluctuating magnetic field inhomogeneities, neighboring spins precess at slightly different resonance frequencies. This leads to a loss of phase coherence, and the magnetization in the transverse plane decays exponentially to zero. The time by which about 63% of the original transverse magnetization has decayed is called transverse relaxation time T_2. Slowly moving protons are more affected by field inhomogeneities and therefore have shorter T_2 relaxation times than fast moving protons. Therefore, different tissues have different T_2 relaxation times and thus different signal intensities in T_2-weighted MR images.

T_2^* relaxation

Not only fluctuating magnetic fields created by molecular motion affect the dephasing of spins. Static magnetic field inhomogeneities, e.g. caused by air-tissue interfaces or biological tissue inhomogeneities, also accelerate spin dephasing. If both fluctuating and static magnetic field inhomogeneities are taken together, the time constant by which 63% of the original transverse magnetization has decayed, is called T_2^*.

$$\frac{1}{T_2^*} = \frac{1}{T_2} + \frac{1}{T_2'} \tag{1.3}$$

Here, T_2' stands for the dephasing caused by fluctuating magnetic fields.

Relaxation rate

Apart from the relaxation time constants, also the relaxation rate is a frequently used term and is defined by

$$R_{1,2}^{(*)} = \frac{1}{T_{1,2}^{(*)}} \tag{1.4}$$

1.2.3 MRI contrast agents

In MRI, contrast arises from the intrinsic T_1 and T2 relaxation times, but contrast agents can be used to shorten these relaxation times and thereby change the image contrast. Commonly, contrast agents are injected intravenously (i.v.), distribute in the body and change the magnetic environment of neighboring protons. The relaxation rate is linearly dependent on the contrast agent concentration C [63-66]

$$R_{1,2} = R_{10,20} + r_{1,2}C \tag{1.5}$$

where $R_{10,20}$ is the longitudinal or transverse relaxation rate without contrast agent and $r_{1,2}$ is the relaxivity r_1 or r_2 of the contrast agent in units of $(mmol/l)^{-1}\ s^{-1}$, which is characteristic for a contrast agent at a fixed magnetic field strength and temperature. There are different types of contrast agents of various sizes and relaxivities.

Paramagnetic contrast agents

Paramagnetic contrast agents are based on paramagnetic metal ions, of which gadolinium (Gd^{3+}) is the most widely used one with 7 unpaired electrons and a high paramagnetic moment, which shortens the relaxation time of neighboring protons. [67]. Due to the high toxicity of free Gd^{3+}, it is used in chelated form in contrast agent complexes. The ratio r_2/r_1 is relatively low for paramagnetic contrast agents, which makes them attractive for signal enhancement (or generation of 'positive contrast') in T_1-weighted images [68].

Superparamagnetic contrast agents

Superparamagnetic contrast agents are ususally iron oxide particles containing thousands of iron ions, which form a strong magnetic moment when placed into an external magnetic field [67]. These particles have very high r_2, which makes them excellent T_2 and T_2^* contrast agents, also called 'negative contrast agents' [68].

1.2.4 Spatial encoding

In MRI we measure the signal from the whole sample or body in the receiver coil and the signal needs to be spatially encoded to provide 2D or 3D images of the sample. By imposing spatially varying magnetic field gradients on the sample in three orthogonal

directions, we can change the resonance frequencies along these gradients. Commonly, a slice selecting gradient is turned on while the excitation pulse is applied to excite only a single slice of the subject with matching resonance frequencies. During signal acquisition, a frequency encoding gradient orthogonal to the selected slice is applied such that the frequency of each proton spin depends on its location along the gradient direction. Before signal acquisition, we apply a phase encoding gradient along the third dimension to impose a spatial variation in the phase of the proton spins. The signal is acquired many times while varying the phase encoding gradient amplitude, and the rate at which the phase varies depends on the location of the signal. This phase encoding step is mostly responsible for the relatively long MRI signal acquisition times, since the image resolution depends on the number of phase encoding steps. From the frequency information we obtain spatial information using Fourier transforms and receive an MR image.

1.2.5 MRI pulse sequences

In MRI, sequences of rf-pulses and magnetic field gradients are used to obtain an image and the sequences can be altered depending on the desired contrast.

Spin echo sequence

A frequently used pulse sequence is the spin echo sequence in which a 90°-pulse is used for excitation and a 180°-pulse for spin refocusing (**Fig. 5**). A $90°_x$-pulse flips the magnetization around the x' axis so that it points along the y'. The signal decays exponentially due to dephasing of the spins within each voxel caused by magnetic field inhomogeneities. A $180°_y$-pulse rotates the dephasing magnetization vectors around the y' axis. In the case of static magnetic field inhomoeneities, the protons retain their precession frequency and the magnetization vectors will rephase and create an echo, which is the recorded signal, at the time TE (echo time). Dephasing caused by fluctuating magnetic field inhomogeneities cannot be rephased and the signal decays with the time constant T_2. This pulse sequence is repeated after the repetition time (TR) to enable phase encoding using varying gradients for each repetition.

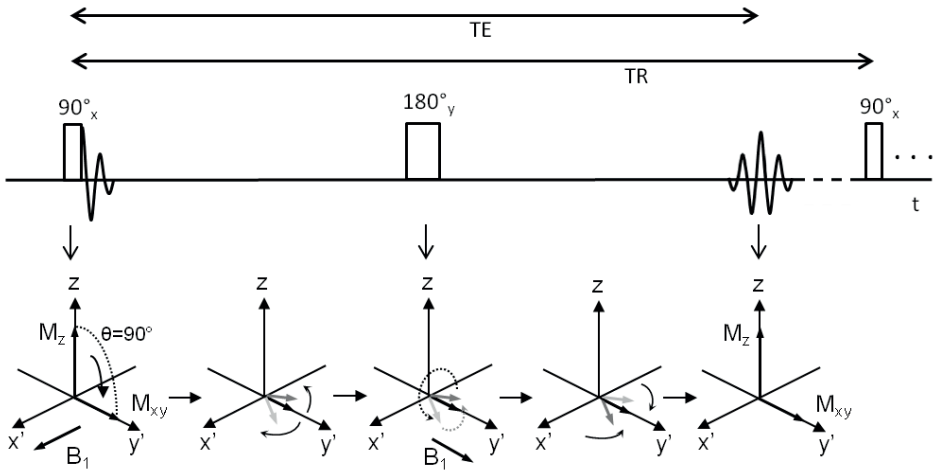

Figure 5: Schematic description of the spin echo pulse sequence and the effect on the magnetization. Here the rotating frame is used for visualization, where the coordinate system is rotating around z at the Larmor frequency so that the precession of M_{xy} around z can be neglected. The x and y axes in this frame are marked as x' and y'.

Acquisitions using the spin echo sequence are time consuming, since TR has to be chosen according to the T_1 of the sample so that the longitudinal magnetization has recovered sufficiently. The data acquisition can be accelerated by the application of several 180°-pulses within one TR. After each 180°-pulse, an echo is formed and can be acquired with a different phase encoding. This modification is called rapid acquisition with refocused echoes (RARE) in which the RARE factor specifies the number of echoes per TR.

The spin echo signal intensity S can be expressed as

$$S \sim \rho_p \left(1 - e^{-\frac{TR}{T_1}}\right) e^{-\frac{TE}{T_2}} \tag{1.6}$$

with ρ_p being the proton density and T_1 and T_2 depending on the imaged sample or tissue. By changing TR and TE, the images can be weighted for T_1 or T_2. A short TR and TE results in T_1-weighted images and a long TR and TE results in T_2-weighted images.

Gradient echo sequence

Another frequently used pulse sequence is the gradient echo. Here, shortly after the 90° excitation pulse, a gradient is switched on and accelerates dephasing of the magnetization. This is followed by a rephasing gradient of opposite direction, which rephases the spins to form an echo. This pulse sequence is faster than the spin echo sequence, but prone to signal loss caused by static field inhomogeneities of the main B_0 field, since there is no 180°-pulse. The signal therefore decays with the time constant T_2*. This feature can be utilized for certain applications such as susceptibility contrast imaging (see **Chapter 1.2.8**).

1.2.6 Diffusion weighted MRI

Diffusion is the Brownian motion of molecules due to their thermal energy above absolute zero. With diffusion weighted (DW) MRI, this diffusion can be measured indirectly as a signal loss induced by diffusion sensitizing gradients applied during the MRI pulse sequence. The use of such gradients in a spin echo sequence is referred to as a Stejskal-Tanner sequence [69] for which a simplified pulse diagram is shown below (**Fig. 6**).

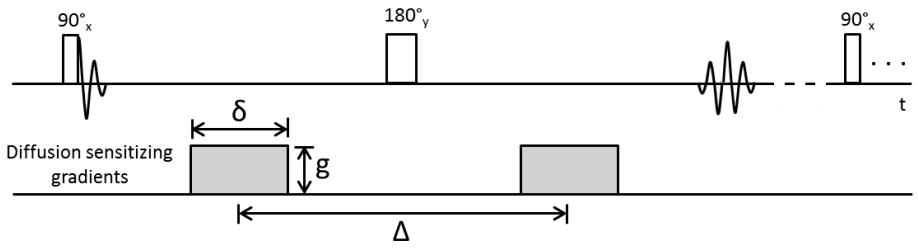

Figure 6: Stejskal-Tanner pulse sequence with two diffusion sensitizing gradients added to the spin echo sequence. The strength of the gradients is g, the gradient duration is δ and the time between the gradients is Δ.

The first gradient induces a phase shift in the spins, which is reversed with an identical gradient applied after the 180°-pulse. However, the spins can only rephase completely if they are stationary between the applications of the two gradients, because moving spins will experience a rephasing gradient that differs from the dephasing gradient. The faster the spins diffuse, the larger is the net displacement of the spins between the gradients

and the lower is the signal of the spin echo. The signal attenuation depends both on the diffusion and the pulse sequence characteristics and the relation can be expressed as

$$S = S_0 e^{-b \cdot ADC} \tag{1.7}$$

where S is the measured signal intensity and S_0 the intensity without diffusion sensitization. The apparent diffusion coefficient (ADC) is what we measure as diffusion, but may also include flow or gross motion, which is why we call it the 'apparent' diffusion coefficient.

The parameter b, referred to as 'b-value' indicates how strong the diffusion sensitization is and depends on the gyromagnetic ratio γ, the gradient strength g, gradient duration δ and time between the two gradients Δ.

$$b = \gamma^2 g^2 \delta^2 (\Delta - \frac{1}{3}\delta) \tag{1.8}$$

To account for potential diffusion anisotropy, the gradients are often applied in three orthogonal directions and the signal of these three acquisitions is averaged. To compute the ADC, a set of MRI images is acquired for at least two different b-values and the ADC value is derived by exponential fitting.

Contrast in DW-MRI arises from the different compositions of biological tissue, because water diffusion is restricted e.g. by cell membranes, macromolecules or other tissue components. Cancerous tissue usually has lower diffusivity compared to normal tissue, which is associated with a higher cell density of tumors, among other factors [70]. Expectedly, ADC has often been shown to be negatively correlated with cell density [71-73]. This property has made ADC a potential imaging biomarker for cancer detection and characterization and for assessment of treatment response. Treatment can change various features of tissue and cells. Cell death can be induced, which leads to a loss of cell membrane integrity and decreased cell density and may lead to increased diffusion as visualized in **Fig.7**.

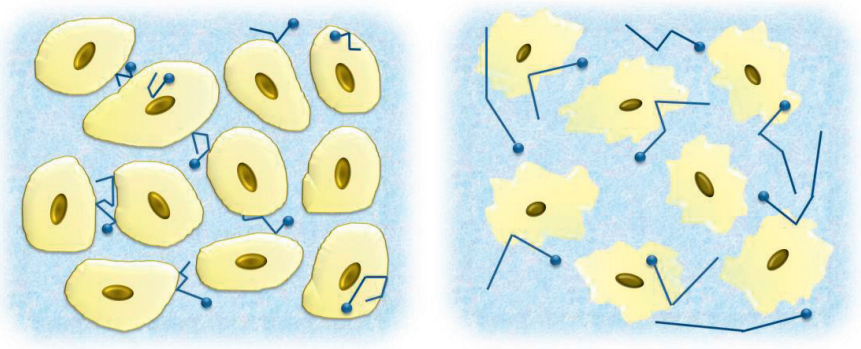

Figure 7: Left: Free water diffusion is hindered by hydrophobic cell membranes of cells that are tightly packed. Right: Degenerative cell changes lead to lower cell density and cell membrane disintegration, allowing water to diffuse more freely.

An increase in ADC is often reported after tumor treatment [74], but also decreases in ADC have been reported and may be attributed to cell swelling or the reduction of edema [75]. Although DW-MRI is already frequently added to conventional MR imaging protocols in oncology, a standardization of both DW-image acquisition (e.g. choice of b-values) and analysis (e.g. mono-exponential vs multi-exponential fitting) is still needed [70]. In addition, the extent and timing of changes in ADC upon treatment need to be more reliably characterized before ADC can become a valid biomarker for treatment response [70].

1.2.7 Dynamic contrast-enhanced MRI

With dynamic contrast-enhanced (DCE) MRI the distribution of a positive contrast agent in the tissue can be followed over time by acquiring a series of images with identical geometry before and at several time points after contrast agent administration.

The distribution of intravenously applied contrast agents in the tissue depends on perfusion and extravasation out of the blood vessels. DCE-MRI can therefore be used for cancer diagnosis due to vascular differences in normal and cancerous tissue. The shape of the signal enhancement curve depends on the tissue characteristics. For malignant tumors, the signal intensity vs. time curve is usually characterized by a fast signal enhancement, followed by a slow wash out of contrast agent from the tissue (**Fig. 8**). The signal enhancement curve can be described by model-free parameters

characterizing the kinetics of the contrast agent in the tissue. These parameters include time to peak enhancement (TTP), fraction of enhancing voxels (FEV), the relative signal enhancement (RSI) and area under the enhancement curve (AUC).The latter two are typically measured at set time points, e.g. 1 min post contrast administration.

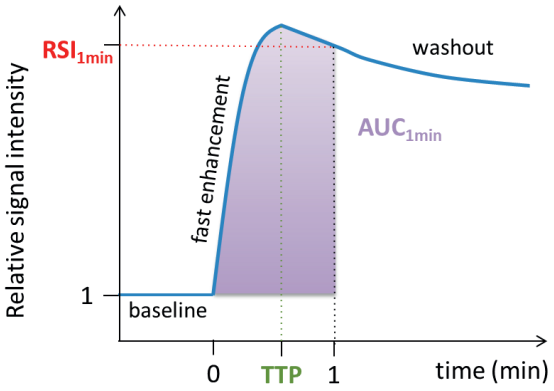

Figure 8: Signal enhancement curve showing the pre-contrast baseline signal and the fast signal enhancement upon contrast agent injection, which is followed by a slower washout. Semi-quantitative parameters describing the enhancement curve are illustrated. TTP: time to peak, RSI_{1min}: relative signal intensity 1min after contrast administration, AUC_{1min}: area under signal enhancement curve 1 min after contrast administration - often referred to as initial area under the curve (IAUC).

There are also numerous approaches for quantification of DCE-MRI data by compartment modelling. These approaches usually lead to an estimation of parameters, of which some are related to physiological characteristics.

The extended Tofts-model is a frequently applied two-compartment model that assumes that the contrast agent is either intravascular or can diffuse into the extravascular extracellular space (EES) but remains extracellular [76] (**Fig. 9**).

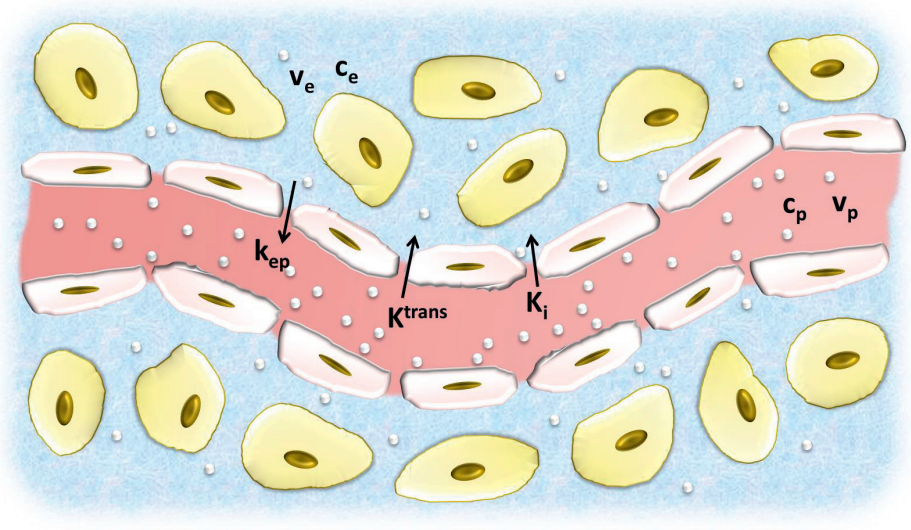

Figure 9: Contrast agent flowing through a blood vessel and leaking out into the interstitium. Abbreviations: c_p - contrast agent concentration in the blood plasma, v_p – blood plasma volume per unit volume of tissue, c_e – contrast agent concentration in EES, v_e - volume of EES per unit volume of tissue, K^{trans} and K_i - volume transfer constants between blood plasma and EES, k_{ep} - rate constant between EES and blood plasma.

With the generalized form of the Tofts-model, three parameters can be estimated: K^{trans} is the volume transfer constant between blood plasma and EES, v_e is the volume of EES per unit volume of tissue, and v_p is the blood plasma volume per unit volume of tissue [76,77]. Under mixed flow- and permeability-limited conditions, K^{trans} depends on capillary permeability, vessel surface area and blood flow in the tissue [76]:

$$K^{trans} = Ef \cdot F \cdot \rho_t \cdot (1 - Hct) \tag{1.9}$$

where Ef is the extraction fraction, F the blood flow per unit mass of tissue, ρ_t the tissue density and Hct the blood hematocrit [76]. Alternative notations include

$$K^{trans} = (1 - Hct)K_i = k_{ep} \cdot v_e \tag{1.10}$$

where K_i represents the transfer constant from plasma to EES and k_{ep} the rate constant between EES and blood plasma [76,78].

In the Tofts-model, the estimated parameters K^{trans}, v_e and v_p are derived from the time dependent contrast agent concentration in the tissue $C_t(t)$ and in the blood plasma $C_p(t)$ according to [76,77]

$$C_t(t) = K^{trans} \int_0^t C_p(\tau) \cdot e^{-(K^{trans}/v_e)(t-\tau)} d\tau + v_p \, C_p(t) \qquad (1.11)$$

$C_t(t)$ can be derived from the signal enhancement curve measured with DCE-MRI. To convert the signal S(t) to $C_t(t)$, knowledge of the dependence of the signal on the MR pulse sequence is necessary. In the case of a T_1-weighted spin echo sequence, the signal depends mostly on T_1 (see equation 1.6), which in turn is linearly dependent on the contrast agent concentration in the tissue according to (1.5). The baseline T_1 relaxivity of the tissue, T_{10}, can be determined by pre-contrast T_{10}-mapping using a separate pulse sequence. The ratio of the signal S to the baseline signal S_0 from (1.6) together with (1.5) can then be used to determine C_t (t). The contrast agent concentration in the plasma $C_p(t)$ is usually referred to as the vascular or arterial input function (VIF or AIF) and needs to be measured separately e.g. by MRI [79,80] or blood sampling [81]. In many cases it is challenging or too time consuming to acquire a VIF for each patient, so often population based VIFs are utilized, although this may leads to a bias in the computation of K^{trans}, v_e and v_p [80].

DCE-MRI is increasingly used in drug trials for monitoring of tumor vasculature. For the assessment of response to drugs directly or indirectly targeting the vasculature it is necessary to derive quantitative parameters [82]. K^{trans} and AUC are frequently reported values in studies quantifying changes in tumor vasculature [83]. However, the dependence of these parameters on both blood flow and vessel permeability makes interpretation of how such parameters correlate with tumor physiology and vascular function difficult. Moreover, a standardization of both data acquisition and analysis is desirable so that data is comparable between studies.

1.2.8 Steady state susceptibility contrast MRI

Steady state susceptibility contrast (SSC) MRI can be used for the indirect assessment of vascular characteristics within a voxel. Here, usually superparamagnetic contrast agents are used due to their high r_2 values [67].

Intravascular superparamagnetic iron oxides lead to an increased difference in magnetic susceptibility between blood vessels and the surrounding tissue. This leads to magnetic field gradients, which cause an increase of both R_2 and R_2* relaxation rates and consequently a signal loss after administration of the contrast agent. The relaxation rates increase with contrast agent concentration, but are also dependent on the vascularization of the tissue [84]. For instance, R_2* increases with increasing fractional blood volume (FBV) of the tissue, while R_2 increases only slightly [84]. Tropres et al. have derived an expression for the estimation of the fraction of blood volume in the tissue (FBV) depending on the difference of R_2* in an MRI voxel before and after contrast agent administration [85]

$$FBV = \frac{3}{4\pi}\frac{\Delta R_2^*}{\gamma \Delta \chi B_0} \tag{1.12}$$

in which γ is the gyromagnetic ration of the ^{1}H nucleus, $\Delta\chi$ the susceptibility difference between blood with and without contrast agent and B_0 the strength of the external magnetic field. Similarly, ΔR_2 and ΔR_2* can be used to estimate vessel size [85,86] or blood vessel density [87].

Currently, SSC-MRI is not widely used in humans, because clinically approved contrast agents have short blood plasma half-lives. However, this method may become of interest when suitable contrast agents become available. A compound that would make a suitable contrast agent is ferumoxytol, a superparamagnetic iron oxide with long circulation half-life, which is used to treat iron deficiency anemia in patients with chronic kidney disease. Recently, ferumoxytol has been used off-label in clinical SSC-MRI studies [88,89].

1.3 X-ray computed tomography

X-ray computed tomography (CT) was introduced in the early 1970s by Allan MacLeod Cormack and Godfrey Newbold Hounsfield [90,91]. For their work, they received the Nobel Prize in Physiology or Medicine "for the development of computer assisted tomography" in 1979.

The image contrast in CT arises from the varying X-ray attenuation properties of different types of tissue. The attenuation of a monoenergetic X-ray beam by a homogenous substance is described by the Lambert-Beer law:

$$I(x) = I_0 e^{-\mu x} \tag{1.13}$$

with I_0 being the intensity emitted by the X-ray source and I(x) the X-ray intensity after traversing a distance x through a material with an attenuation coefficient μ. Importantly, μ is dependent on the X-ray energy and the density and atomic number of the material. For example, bones attenuate X-rays more than soft tissue. For inhomogeneous material, such as biological tissue, the signal intensity can be written as an integral in which the attenuation coefficient varies for different locations x along the path:

$$I(x) = I_0 e^{-\int \mu(x) dx} \tag{1.14}$$

If the object is scanned at a fixed angle, a 2D X-ray image is created in which the image intensity represents the average absorption in the beam direction. To gain depth information, the object needs to be scanned at different angles over 180 degrees from which a 3D volume is created after tomographic image reconstruction, which is described in detail in [92].

For CT of small animals or specimen, bench-top micro-CT (μCT) scanners are available that achieve images with isotropic voxel sizes down to ~1μm [93,94]. Scanners using synchrotron radiation can acquire images at even lower resolution but are of higher financial cost and limited availability, so they cannot be used routinely for large scale experiments [94]. The availability of (μCT) scanners and their use in preclinical research have greatly increased for the past decade [95-97].

µCT for vascular imaging

Preclinical applications of µCT include bone, lung, cardiac and vascular imaging [95,97]. High resolution structural imaging of blood vessels in 3D on the whole tumor level and without tissue destruction can be best performed by µCT [93]. *In vivo* imaging is often advantageous over *ex vivo* imaging, especially because it allows for longitudinal studies and recapitulates the true *in vivo* environment. However, the *in vivo* µCT resolution is not sufficient to image the smallest capillaries, which can be as small as 4µm in diameter in mice [98], so *ex vivo* imaging is performed when very high resolution is desired.

Since CT provides very low endogenous contrast between blood vessels and surrounding tissue, contrast agents of high radio-density have been developed. For *ex vivo* imaging, animals are commonly perfused with the contrast agent via the still beating heart. After perfusion, the contrast agent is required to solidify. Other contrast agent properties required for an exact analysis of the vascular network include a low viscosity for complete filling of small vessels, absence of extravasation, and limited shrinkage upon hardening [93].

One frequently used contrast agent is Microfil (MV-series) (Flow Tech, Inc., Carver, MA, USA), a lead-containing silicone rubber that polymerizes approximately 90 minutes after mixing with a curing agent with very little shrinkage. This method allows the intact tumor to be scanned by µCT after which other analyses such as histopathology can be performed. One disadvantage is, however, that background signal from the tumor tissue can make segmentation of small vessels challenging. Microfil has been used to compare the vascularization of different tumor models [99] or assess treatment-induced vascular changes [100-103].

1.4 Histopathology

Histopathology refers to the study of the cytology and structure of diseased tissue at the microscopic level. Today, the histopathological examination of tissue biopsies is a standard for the diagnosis of cancer.

Tissue samples are commonly sectioned into thin slices (commonly 4µm thick) and stained to visualize cellular components or provide contrast between different structures. A frequently used staining technique is called H&E, utilizing a combination of hematoxylin, which stains cell nuclei blue, and eosin, which stains cytoplasm pink. In addition, saffron can be used to stain collagen fibers yellow. This triple stain is called HES. Both techniques produce stains suitable for a cellular characterization of cancer tissue using light microscopy.

It is also possible to stain antigens in the tissue with antibodies conjugated to fluorescent probes or enzymes with chromogenic or fluorescent substrates. This technique is called immunohistochemistry.

1.5 Intravital microscopy

While histopathology allows imaging of tumor features at subcellular resolution, this method needs to be performed *ex vivo*, which precludes the longitudinal study of physiological processes. The previously discussed *in vivo* imaging modalities such as MRI and CT can be performed at various time points. However, they lack the resolution for imaging at the cellular level. Intravital microscopy (IVM) is a unique method for repeated microscopic *in vivo* imaging of intact tissue and has been an invaluable tool for the study of gene expression, angiogenesis, blood flow, vascular permeability, pH, transport of molecules and cells, cell-cell interactions and other biological processes in tumor models [16,104-106]. IVM requires tissue preparation, an optically detectable probe and a microscope [107].

Window chamber models are a way of preparing tissue so that the area of interest can be observed through a glass window, which is surgically implanted into the dorsal skin flap or cranium [16]. Dorsal window chambers are frequently used to look at normal tissue or tumors. A dorsal skin flap is prepared by dissecting away one side of the skin flap so

that the vasculature and connective tissue of the other side become visible and is covered by a glass. A frame holds the skin flap and glass cover in place [105]. This setup enables the study of normal blood vessels. Alternatively, tumor cells can be grown underneath the glass for the study of tumor tissue or vasculature. While dorsal window chambers are a superb technique for high resolution imaging of many physiological features of tumors, there are some important limitations. First, tumors grown in window chambers may differ from orthotopically grown tumors due to a different tumor environment [108]; and second, only a thin tumor of up to about 500 μm can be grown below the glass cover, so that necrotic or hypoxic regions, which are frequently observed in orthotopic or subcutaneous tumours, rarely form [106].

Frequently used optical probes are, for instance, fluorescent drugs to study pharmacokinetics, probes responding to changes in pH to study the tumor microenvironement or probes targeting certain receptors to quantify receptor expression and binding [107].

Advanced fluorescent microscopy techniques such as confocal laser scanning microscopy or multiphoton microscopy enable 3D imaging due to their ability to focus on selected planes at different tissue depths [106]. However, the penetration depth of light in tissue is limited to about 1mm [109].

1.6 Multifunctional nanoparticles

In recent years, advances in nanotechnology have made it possible to design multifunctional nanoparticles that can be used for a large variety of applications such as molecular imaging and drug delivery.

One group of such particles are lipid based, consisting mainly of amphiphilic lipids which consist of a polar head group (hydrophilic) and a non-polar tail (hydrophobic). In an aqueous environment, amphiphiles spontaneously assemble into aggregates such as micelles or liposomes. A mixture of lipids, water and oil is the basis for the formation of emulsions, one type being oil-in-water nanoemulsions, which consist of an oil core separated from water by a lipid monolayer [110].

The shape and size of these aggregates depends on the size and charge of the hydrophilic and hydrophobic parts and the environment (e.g. pH, temperature, concentration). The aggregation is driven by water's repulsive interactions with the hydrophobic parts and associative interactions with the hydrophilic parts. Phospholipids are often used for the synthesis of nanoparticles [111] and are also the main constituents of biological cell membranes.

Nanoparticles can serve multiple functions. One is the delivery of drugs to solid tumors through 'passive targeting'. Nanoparticles can leak out and accumulate in tumors due to the high permeability of tumor vessels to macromolecules, which cannot pass the walls of blood vessels in normal tissue, and the limited lymphatic drainage in tumors. This is called the "enhanced permeability and retention (EPR) effect" [112]. This effect is exploited, for example, to treat ovarian cancer with liposomal doxorubicin [10]. Another application of high interest is molecular imaging. Nanoparticles can contain contrast agents for MRI such as gadolinium or iron, which affect the relaxation times. They can also be fluorescently labeled, which allows for their detection using various fluorescence microscopy techniques [111]. In addition, targeting ligands can be conjugated to nanoparticles, which enables 'active targeting' of nanoparticles to specific cell receptors [111].Several of these functionalities can be combined when designing nanoparticles, which makes them very versatile and allows them to be tailored for a variety of preclinical applications.

2 Aims

The main objectives of this thesis were to develop and assess the performance of multi-modal imaging methodologies for characterizing physiological tumor features and their changes induced by treatment. More specifically, the goals were to:

- develop co-registration procedures for multi-modal imaging of tumor vasculature.

- assess the performance of *in vivo* MR imaging biomarkers for tumor cellularity, vascular morphology and vascular function by comparison with suitable *ex vivo* imaging methods.

- characterize the cellular and vascular response of two different ovarian cancer xenograft types to PI3K/mTor inhibition.

- develop multi-modal imaging procedures for assessing nanoparticle targeting kinetics *in vivo* on the whole tumor level.

3 Materials and methods

This thesis comprises three papers in which various imaging methods were used to quantify characteristics or treatment response of human cancer xenografts. The material and methods used in these studies are summarized in **Table 1**.

Table 1 Summary of materials, methods and data analysis techniques used in papers I-III

		Paper I	Paper II	Paper III
Materials	Cell lines	MDA-MB-231	TOV-112D TOV-21G	TOV-112D HUVEC
	Drugs	-	BEZ235	-
	MRI contrast agent	Feridex	Omniscan	Nanoemulsion containing Gd-DTPA
Methods	*in vivo* MRI	SSC-MRI DW-MRI	DCE- MRI DW-MRI	DCE-MRI
	ex vivo MRI	micro- MRI	anatomical MRI	-
	ex vivo µCT	CT angiography	CT angiography	-
	IVM	-	-	vascular input function
	Histopathology	-	HES Ki-67	CD31 DAPI
	Protein expression	-	Western blotting	-
Data analyses	DCE-MRI	Tofts	-	Tofts
	SSC-MRI	FBV	-	-
	DW-MRI	monoexponential fitting	monoexponential fitting	-
	CT angiography	FBV	FBV, vessel density, radius, length	-

Abbreviations: HUVEC: human umbilical vein endothelial cells, Gd-DTPA: Gadopentetic acid, MRI: magnetic resonance imaging, SSC: steady state susceptibility contrast, DCE: dynamic contrast enhanced. DW: diffusion weighted, CT: computed tomography, IVM: intravital microscopy, HES: Hematoxylin-Eosin-Saffron, FBV: fractional blood volume

3.1 Cell lines and animal models

In all three papers, cell line-derived xenografts were grown in immunodeficient nude mice. In paper I the animal experiments were conducted in accordance with the Animal Care and Use Committee guidelines at the Johns Hopkins University, Baltimore, MD, USA. For paper II and III all animal procedures were approved by the Norwegian Animal Research Authority, and carried out according to the European Convention for the Protection of Vertebrates used for Scientific Purposes.

3.1.1 MDA-MB-231 human breast cancer cell line

The MDA-MB-213 breast cancer cell line was isolated from a pleural effusion of a 51 year-old breast cancer patient in 1973 [113]. Today, this aggressive cell line is well characterized and one of the most widely used breast cancer cell lines in research experiments [114,115]. The cells express high levels of VEGF *in vitro* and xenografts established from these cells are reported to be well vascularized [115].

For paper I, MDA-MB-231 cells were grown in RPMI-1640 medium supplemented with 10% fetal bovine serum and penicillin-streptomycin. Xenografts were grown orthotopically in female athymic NCr nu/nu mice after injection of three million cells in to the left thoracic mammary fat pad.

3.1.2 TOV-21G and TOV112D human ovarian cancer cell lines

The two ovarian cancer cell lines used in this work were established directly from malignant ovarian tumors of different clinical phenotypes. The TOV-21G cell line originates from a clear cell carcinoma while the TOV-112D cell line was derived from an endometrioid carcinoma [116].

In paper II, TOV-21G and TOV-112D cells were characterized for their PI3K signaling activity and xenografts were grown for *in vivo* imaging by injection of five million cells subcutaneously into the hind limb of female athymic BalbC nu/nu mice. For paper III only TOV-112D xenografts were used. The cells were grown in a 1:1 mixture of Medium 199 (Gibco 41150) and MCDB 105 Medium (Sigma M6395) supplemented with 15% fetal bovine serum and 0.05mg/ml gentamicin.

3.2 Drug BEZ235

NVP-BEZ235 (or BEZ235) is a dual pan-class I PI3K and mTOR kinase inhibitor developed by the Global Discovery Chemistry Group (Novartis Pharma, Novartis Institutes for Biomedical Research Oncology) [33]. Inhibition of both mTORC1 and mTORC2 has been reported [33]. The drug has reached phase 2 clinical trials (clinicaltrials.gov).

For paper II, BEZ235 was purchased from LC Laboratories, Woburn, MA, USA and dissolved to 14 mg/ml in dimethyl sulfoxide (DMSO, Sigma-Aldrich #D-5879) under gentle heating. It was then diluted to a final concentration of 6.5mg/ml using polyethylene glycol (PEG300, Sigma-Aldrich #20237-1) and administered to the mice at a dose of 65 mg/kg/day by oral gavage on three consecutive days.

3.3 *In vivo* MRI

In all three papers, in vivo MRI was used to image tumor xenografts grown in mice. An overview of the MR sequences for each paper is given in **Table 2**.

3.4 µCT

For paper I, µCT of breast xenografts was performed to validate *in vivo* MRI data and measure the FBV. For paper II, µCT of ovarian xenografts was conducted to measure FBV, vessel radius, length and density. In both papers, mice were perfused intracardially with saline, followed by formalin and Microfil. The compound polymerizes after the perfusion to form a radio-opaque vascular cast.

Micro-CT was performed by Numira Biosciences (Salt Lake City, UT, USA) on a high-resolution, volumetric µCT scanner (µCT40, ScanCo Medical, Brüttisellen, CH). All images were acquired at 8 µm isotropic resolution with 55 kVp, 300 ms exposure time, 2000 views and 5 frames per view.

3.5 Oil-in-water nanoemulsions

In paper III, multi-functional and multi-modal oil-in-water nanoemulsions were used for targeting and imaging of $\alpha_v\beta_3$ integrin in angiogenic tumor blood vessels. The nanoparticles were synthesized by Sjoerd Hak and characterized and described in a previous paper [117]. The nanoemulsion consists of a soybean oil core and a phospholipid mixture forming a monolayer, stabilized by cholesterol. For MR-contrast, the headgroups of one phospholipid type contained gadolinium. For intravital imaging and histology, the nanoemulsions contained two types of fluorescent molecules in the oil core and the headgroups of the phospholipids, respectively. The nanoparticles were conjugated to RGD, which served as a targeting ligand to $\alpha_v\beta_3$ integrin.

Table 2 Detailed MRI sequence parameters used in papers I-III

	Paper I	Paper II	Paper III
Hardware			
MR scanner	Bruker Biospin	Bruker Biospec	Bruker Biospec
field strength	9.4T	7.05T	7.05T
transmit coil	18mm solenoid	72mm volume	72mm volume
receive coil		quadrature surface	quadrature surface
Geometry			
FOV (mm^2)	14 × 14	23 × 23	25.2 ×14.4
slice thickness (mm)	1	0.692	1
interslice distance (mm)	1	1	n.a.
number of slices	3-8	5	1
high resolution images			
sequence		RARE spin-echo	FLASH
TR (ms)		2000	350
TE (ms)		12	5.4
RARE factor		8	n.a.
Matrix		256 × 256	224 × 128
in plane resolution (µm)		90	112.5
number of averages		1	8
DW-MRI			
sequence	RARE	EPI	
Preparation mode	spin-echo	spin-echo	
TR (ms)	1000	3000	
TE (ms)	26.6	28	
b-values (s/mm^2)	0, ~300	0, 100, 300, 600, 1000	
Matrix	128 × 128	64 × 64	
in plane resolution (µm)	100	359	
number of averages	2	1	
number of segments	n.a.	4	
gradient orientations	3 orthogonal	3 orthogonal	
DCE-MRI			
Matrix		64 × 64	56 × 32
in plane resolution (µm)		359	450
T1-map			
sequence		RARE	RARE
TR (ms)		150, 750, 1500, 2500, 4500, 1200	150, 750, 1500, 2500, 4500, 12500
TE (ms)		7.2	7
RARE-factor		2	2
zerofill accelleration		1	1.34
number of averages		1	1
Dynamic series			
sequence		RARE	RARE
TR (ms)		300	300
TE (ms)		7.2	7
RARE-factor		4	2
temporal resolution (s)		4.8	21.6
number of repetitions		200	60
number of averages		1	6
zero fill accelleration		1	1.34
Injection			
Gd Dose (mmol/kg)		0.3 (Omniscan)	0.02 (in nanoemulsions)
baseline scans		10	5
injection duration (s)		~ 4	~ 20
SSC-MRI			
sequence	MGE		
TR (ms)	800		
TE (ms)	4.2, 7.2, 10.2, 13.2, 16.2, 19.2		
flip angle (°)	90		
number of averages	4		
Matrix	128 × 128		
in plane resolution (µm)	100		
iron dose mg/kg	25 (Feridex)		

Abbreviations: FOV: field of view, TR: repetition time, TE: echo time, RARE: rapid acquisition with relaxation enhancement, FLASH: fast low angle shot, MGE: multi-echo gradient-echo, EPI: echo planar imaging

3.6 Intravital microscopy

For paper III, IVM was used to acquire a vascular input function for DCE-MRI analysis using the fluorescent nanoemulsion labeled with GD-DTPA. The window chamber preparation was performed at the Department of Physics (NTNU) and confocal microscopy for the acquisition of the VIF was performed by Sjoerd Hak.

3.7 Histopathology

For paper II, histopathology of treated and untreated xenografts was performed to assess changes in cell morphology and proliferation after PI3K/mTOR inhibition. Cell morphology was qualitatively assessed in HES stained sections. Sections were also stained for Ki-67, which is a protein present only in proliferating cells [118] and the density of stained cell nuclei was visually assessed.

In paper III, histology was performed to assess the distribution of nanoemulsion in tumor tissue in relation to blood vessels. The protein CD-31 (also called PECAM-1) is a cell adhesion molecule highly expressed by endothelial cells [119] and was fluorescently stained to visualize blood vessels. Cell nuclei were counterstained with 4',6-diamidino-2-phenylindole (DAPI), which is a probe binding specifically to a certain DNA sequence, upon which it forms a fluorescent complex [120]. The fluorescence was detected using an inverted fluorescence microscope Olympus IX71 and images were acquired using a 20X objective.

3.8 Protein Expression

For paper II, protein expression of TOV-112D and TOV-21G tumor cells was analyzed using western blotting by Prof. Bjørkøy's group at Høgskolen i Sør-Trøndelag (HiST). Proteins were separated by electrophoresis and the expression of total Akt, p-Akt, p-S6 and total S6 was detected with specific antibodies and visualized using fluorescent secondary antibodies. The expression of p-Akt was also visualized in histology sections of TOV-112D and TOV-21G xenografts by labelling with fluorescent antibodies. The fluorescent intensity of both cell extracts and xenograft sections was assessed using the Odyssey Infrared Imaging System and Image Studio 3.1 software (LI-COR Biosciences, Lincoln, NE, USA).

4 Summary of papers

Paper I

Multiscale and multi-modality visualization of angiogenesis in a human breast cancer model

Jana Cebulla, Eugene Kim, Kevin Rhie, Jiangyang Zhang and Arvind P. Pathak

Angiogenesis. 2014 Jul;17(3):695-709.

Angiogenesis is of high importance for cancer growth, invasion and metastasis. A better understanding of tumor blood vessel characteristics is therefore necessary, for instance to facilitate the development of new cancer treatment strategies.

In this paper, we developed multiscale and multi-modality imaging techniques for studying tumor blood vasculature in human breast cancer xenografts grown from MDA-MB-231 cells. On the macroscopic scale, we used *in vivo* SSC-MRI to create FBV maps with 100 μm in plane resolution and *in vivo* DW-MRI to acquire complementary information on tumor cellularity. On the microscopic scale, *ex vivo* μCT was performed to image the vasculature at the microvessel level with 8 μm isotropic resolution. Due to the large disparity in spatial resolution, we used *ex vivo* μMRI to aid the co-registration between *in vivo* MRI and μCT. Suitable vessel extraction and intermodality co-registration techniques were developed.

The tumor FBV was computed for each imaging modality. It was found that the FBV derived from both MRI methods was overestimated compared to the μCT although the μMRI and μCT FBV showed the same spatial distribution. Importantly, all three modalities were able to depict the decreased FBV in the tumor center compared to the rim. Finally, we demonstrated an application of our multi-modality imaging approach in which we overlaid the high-resolution μCT tumor blood vessels onto diffusion maps from the *in vivo* MRI data. This way we were able to visualize the poor blood supply in necrotic tumor regions.

The methods developed in this paper can facilitate the integration between multiscale and/or multi-modality data related to angiogenesis in pre-clinical cancer models. Several methods developed here were used in paper II.

Paper II

MRI Reveals the in Vivo Cellular and Vascular Response to BEZ235 in Ovarian Cancer Xenografts with Different PI3-Kinase Pathway Activity

Jana Cebulla, Else Marie Huuse, Kristine Pettersen, Anna van der Veen, Eugene Kim, Sonja Andersen, Wenche S. Prestvik, Anna M. Bofin, Arvind P. Pathak, Geir Bjørkøy, Tone F. Bathen, Siver A. Moestue

Br J Cancer 2015 Feb 3;112(3):504-13.

The purpose of this study was to investigate MRI biomarkers for response to PI3K/mTor inhibition. The cellular and vascular responses of ovarian xenografts to treatment with BEZ235 were measured using MRI, μCT and immunohistochemistry. First, the PI3K activity of the cell lines was measured using immunoblotting, which revealed low PI3K signaling activity in TOV-112D cells and high activity in TOV-21G cells, suggesting that the latter is more responsive to treatment.

After the establishment of subcutaneous xenografts in mice, the tumors were imaged before and three days after treatment with 65 mg/kg BEZ235 using DW-MRI and DCE-MRI. A strong treatment response was found for the TOV-21G xenografts in form of a decrease in tumor volume and decreased cell proliferation, while only a slight growth inhibition was found for the TOV-112D xenografts. DW-MRI measured a strong treatment response in TOV-21G xenografts as ADC values increased significantly. DCE-MRI displayed elevated v_e for both xenograft types and suggested an improved vascular function to a similar extend in both treated xenograft models. Changes in vascular morphology could not be ascertained in this study.

The results of this study suggest that DW-MRI may be a valuable tool for assessing response to PI3K/mTor inhibition *in vivo*. DCE-MRI can give additional information on vascular function and compartment modeling can yield quantitative parameters. However, the physiological meaning of those parameters is often difficult to interpret. In contrast, the diffusion coefficient derived from DW-MRI can be more easily interpreted, which is why we suggest that ADC be further evaluated as a biomarker for response to targeted drugs.

Paper III

Periodicity in tumor vasculature targeting kinetics of ligand-functionalized nanoparticles studied by dynamic contrast enhanced magnetic resonance imaging and intravital microscopy

Sjoerd Hak, Jana Cebulla, Else Marie Huuse, Catharina de L. Davies, Willem J.M. Mulder, Henrik B.W. Larsson, Olav Haraldseth

Angiogenesis. 2014 Jan;17(1):93-107.

In this paper we studied the accumulation of nanoparticles in TOV-112D ovarian xenografts using DCE-MRI. The multi-modality nanoemulsions contained gadolinium-lipids for MR contrast enhancement and a fluorescent dye for IVM. In addition, the emulsions were RGD-conjugated, which enabled them to bind to $\alpha_v\beta_3$-integrin, which are receptors highly expressed on angiogenic endothelial cells.

The *in vivo* nanoemulsion kinetics were studied with DCE-MRI on the whole tumor level. Compartment modeling was performed to quantify the targeting rates of nanoemulsions targeted to $\alpha_v\beta_3$-integrin using the MR contrast enhancement curve and a VIF. For this purpose, dorsal window chambers were implanted on healthy mice and confocal laser scanning microscopy was used to obtain the VIF after injection of fluorescent nanoemulsions. The results were validated by investigating the $\alpha_v\beta_3$-integrin targeting dynamics with HUVEC cells *in vitro*.

DCE-MRI showed that the RGD-conjugated nanoemulsions accumulated faster in the tumor rim compared to non-targeted nanoemulsions. Moreover, a fluctuation was found in the contrast enhancement curve for the targeted but not for the non-targeted nanoemulsion. The *in vitro* experiments strongly indicated that this fluctuation was caused by integrin dynamics, i.e. integrin binding, internalization into cells and recycling to the cell surface.

This study demonstrated that DCE-MRI may be a suitable tool for the investigation of targeted nanoparticle kinetics in cancer. In addition, this method may be a unique tool for the quantification of endothelial cell receptor expression levels and study of integrin dynamics *in vivo*, which are still insufficiently characterized.

5 Discussion

Multi-modal imaging is becoming the standard in clinical cancer care because a combination of complementary data allows for more precise cancer diagnosis and staging, treatment planning and assessment of treatment response. Also for preclinical research, multi-modal imaging is often used in order to characterize physiological properties of tumors in detail. In addition, the development of new, clinically translatable imaging biomarkers often relies on multi-modal imaging for biomarker validation.

In all papers that compose this thesis, several imaging modalities were combined to either take advantage of the complementary information or to validate imaging biomarkers. The multi-modal approaches were then used to explore vascular features of cancer or to assess response to treatment.

5.1 Multi-modal imaging for validating imaging biomarkers

Non-invasive imaging modalities are valuable tools for cancer diagnosis and assessment of treatment response. Especially for novel targeted drugs, for which it is difficult to predict response in individual patients prior to treatment, novel biomarkers for response are needed. Clinical imaging modalities such as MRI, CT and ultrasound have a relatively low resolution that is sufficient for anatomical imaging and measuring tumor size but not for directly visualizing e.g. small capillaries. However, with the use of mathematical modelling and under certain assumptions, we can use these imaging modalities to ***indirectly*** characterize physiological measures such as tumor vascularization (e.g. FBV, vessel size and density), vascular function (e.g. permeability, blood flow) and tumor cellularity.

In this thesis, *in vivo* MRI was used to measure several imaging biomarkers related to vascular or cellular characteristics. All of these biomarkers were derived indirectly from the MR images using data fitting or mathematical modelling. The assumptions that underlie these derivations do not always apply for complex *in vivo* systems. Thus, before these biomarkers can be used clinically, they first need to be validated by other methods that are well-established in the clinic or that can reliably measure the

underlying physiological properties directly. Unfortunately, such validation is usually challenging. Multi-modal imaging exploits the advantages of each imaging modality, but the modalities may show great differences e.g. in resolution or contrast mechanism and can sometimes not be directly correlated. Still, further improvements in co-registration techniques like in paper I and systematic comparison of *in vivo* with *ex vivo* imaging as performed in papers I-III will help to improve the availability of validation tools.

5.1.1 Validating SSC-MRI-derived tumor FBV using µCT

In paper I, SSC-MRI was used to estimate the FBV in breast tumor xenografts and compared to the FBV derived from co-registered µCT images. High resolution µCT has the advantage of visualizing the 3D vasculature in great detail and is therefore frequently regarded as the 'gold standard' for analyzing structural features of tumor vasculature. Our results showed that the distributions of FBV values in the tumors were similar for the SSC-MRI and µCT data. In a follow up study, it was shown that median tumor FBV measured by SSC-MRI was significantly correlated with that measured by µCT [121]. Ungersma et al. performed the same comparison of SSC-MRI and µCT-derived mean FBV but found no correlation, which may be caused by the exclusion of non-viable tissue from the MRI but not the µCT data. In both their and our studies, SSC-MRI overestimated the absolute FBV values in comparison to µCT, and Kim et al. suggested that relative SSC-MRI biomarkers (proportional to a physiologic measure) may be of greater value than SSC-biomarkers with absolute units [121]. This may be important for the clinical use of SSC-MRI biomarkers, as the use of relative biomarkers may still be helpful e.g. for assessing relative changes in the blood vasculature induced by treatment. It should not be forgotten though, that µCT also has methodological challenges as complete filling of the tumor vasculature is not always achieved [122] or, as in our case, the resolution of 8 µm may not be sufficient to visualize the smallest capillaries. This can diminish its value as the 'gold standard'. Still, µCT has clear advantages over histological hot spot analysis and is a powerful technology for assessing vascular morphology.

5.1.2 Validating changes in ADC as a biomarker for cellular response using histology

DW-MRI is sensitive to water motion. It is a relatively fast imaging technique that does not require the application of contrast agent or complex computations to quantify ADC values, to name a few advantages of this imaging modality. DW-MRI is used for cancer detection, but it is also a promising biomarker for treatment response to cytotoxic and antivascular drugs [70]. However, there are no accepted standards for distinguishing between malignant and benign tissue, nor are there validated and quantified relationships between changes in ADC and response to treatment. It is also not clear whether DW-MRI is useful for monitoring response to other targeted therapies, and generally, DW-MRI is not completely understood at the cellular level [70]. In paper II, we therefore validated treatment-induced changes in ADC with histology. Treatment-induced elevation of ADC is often attributed to increased apoptosis [70], but quantification of apoptosis in tissue sections is challenging, because it can be induced through different biochemical mechanisms and can occur at different time points depending on the type of cancer and drugs involved [123]. This makes it difficult to identify a universal biomarker for apoptosis. In paper II, we therefore chose to assess drug induced changes in cellular characteristics by staining for the Ki-67 protein, which is a widely used proliferation marker [118]. Although Ki-67 expression does not necessarily correlate directly with ADC [124,125], it confirmed that the increase in ADC may be caused by changes on the cellular level as cell proliferation decreased markedly. In addition, HES staining confirmed changes in cell density, which ultimately confirmed that increased ADC could be attributed to treatment-induced changes in the cellularity of the tumors and not, for example, altered perfusion.

Overall, verification of histological causes for changes in ADC is challenging but necessary to bring the use of ADC as a biomarker further towards clinical application.

5.1.3 Validating *in vivo* cell targeting kinetics by *in vitro* cell targeting experiments

In paper III, DCE-MRI was used to investigate the spatial distribution of nanoemulsions in ovarian xenografts over time and to potentially estimate particle binding to $\alpha_v\beta_3$ integrin. Conventionally, nanoparticle kinetics are studied *in vitro* by high resolution

methods such as fluorescent microscopy [117], but in this study the advantage of whole tumor coverage by DCE-MRI was exploited. This study was one of the first to use DCE-MRI to look at nanoparticle kinetics, which makes validation of the results especially necessary. One of the main results from the DCE-MRI was that the RGD targeted nanoemulsion showed a periodicity in its accumulation in the angiogenic tumor rim. It was hypothesized that this periodicity was caused by internalization of the nanoemulsion into endothelial cells after binding to $\alpha_v\beta_3$ integrin. To test this hypothesis, the distribution of the multifunctional nanoemulsion was visualized in histological tumor sections by fluorescent microscopy. This showed no clear evidence that the targeted nanoemulsion was internalized by the cells, which may be a result of the tissue handling during histology, in which the washing steps may cause the particles to be removed from the tissue. Therefore, an attempt was made to reproduce the periodicity *in vitro*. Although this was not an imaging experiment, the *in vitro* work confirmed a periodicity in the internalization of targeted nanoemulsion into HUVEC cells. Finally, Hak et al. showed earlier with IVM that the targeted nanoemulsion was located in close proximity to endothelial cell nuclei, which suggests that the nanoemulsion was internalized into the cells [117]. In this case of whole tumor imaging of nanoemulsion kinetics, no other available imaging modality could easily confirm the DCE-MRI results in the ovarian tumor xenografts because optical imaging such as IVM can only be performed using special setups such as window chambers, which can only accommodate thin tumors and could change other tumor properties. Also histology may not be the method of choice for looking at nanoparticle accumulation in tissue post mortem. Therefore, validation had to be performed in experimental setups not using whole ovarian xenografts.

Paper III was one of the first studies to use and attempt to validate the use of DCE-MRI for monitoring *in vivo* targeting kinetics of nanoparticles to $\alpha_v\beta_3$ integrin. The experiments will have to be reproduced and further validated before DCE-MRI can be considered as a modality for studying nanoparticle kinetics and receptor dynamics.

5.2 Multi-modal imaging of tumor vessel morphology and function

Blood vessels are essential for delivering nutrients and oxygen to drive tumor growth, and angiogenesis is one of the hallmarks of cancer. Imaging of tumor vasculature is important for several reasons. First, it can aid the understanding of angiogenic processes and guide the development of new anti-angiogenic drugs. Further, it can be used for tumor detection due to differences between tumor and normal vasculature. And third, it can be used for monitoring of anti-angiogenic therapy and for early detection of drug resistance.

Blood vessels have a large range of sizes with the smallest capillaries having diameters of only 4μm [98]. There are currently no *in vivo* imaging modalities that can accurately visualize a large volume of tissue with its blood vessels at such high resolution. In addition, tumor vasculature differs from normal vasculature in structure and function, and there is no single imaging modality that can simultaneously measure both 3D vascular architecture and vascular function in a whole tumor. Therefore, the use of multiple imaging modalities is commonly employed for studies assessing tumor angiogenesis.

Imaging of the tumor vasculature was the main or a large part of all three papers in this thesis. Collectively, six imaging modalities were used to study tumor vasculature as summarized in **Table 3**. This table also summarizes the advantages and disadvantages of each imaging modality for vascular imaging, as encountered in the three studies.

Table 3: Summary of imaging methods used for characterizing tumor vasculature in this thesis.

	Imaging Modality	Use in papers	Result	Advantages (+) & Disadvantages (-)	reso-lution
Paper III	Histology	visualization of cell nuclei (DAPI stain), endothelial cells (CD-31 stain) and nanoemulsion (containing fluorescent dye)	Results indicate that targeted nanoemulsion was located closely to the endothelial cells while control nanoemulsion extravasated into extravascular space. However, this was not clearly visible. Visualization was potentially hampered by histology processing steps.	+ Possible to co-stain the tissue section with other markers + *Ex vivo* technique that can be combined with *in vivo* imaging modalities - *Ex vivo* staining of vessels cannot differentiate between functional and dysfunctional vessels - no full tumor coverage	µm
Paper III	CLSM	measurement of vascular input function that was used for DCE-MRI modelling	Using IVM, the fluorescent intensity in blood vessels could be measured over time after injection of fluorescent nanoemulsion. The data was converted into a Gd concen-tration/time curve and could be used as VIF for DCE-MRI.	+ Allows real time observation of fluorescent contrast agent kinetics in vasculature and surrounding cells + Quantification of fluorescent intensity in blood vessels is possible - Not usable for large 3D tumors	
Paper I & II	µCT	3D Angiography at 8µm resolution in breast and ovarian tumor xenografts	In paper I, the vasculature was co-registered to *in vivo* MRI and served as 'gold standard' in the comparison of µCT and SSC-MRI-derived FBV. In paper II, FBV, vessel density, vessel radius and branch length were computed. No differences could be found between TOV-21G and TOV-112D and treated and control xenografts.	+ High resolution, 3D volumetric imaging of blood vessels + Whole-tumor coverage without sample sectioning - Successful contrast agent perfusion is necessary but can be complicated e.g. in case of dysfunctional vessels - Vessel segmentation from images can be challenging	8µm
Paper I & II	µMRI	three uses: 1) imaging of vasculature at ~ 40 µm isotropic resolution 2) co-registration 3) soft tissue imaging for masking tumor from µCT data	In paper I, µMRI visualized tumor vasculature at 40µm resolution. It aided in the co-registration of µCT and *in vivo* MRI data due to intermediate resolution and visualization of both vessels and soft tissue. In paper II, µMRI was used to create a tumor mask for the µCT data to distinguish between intra- and peritumoral blood vessels.	+ Excellent soft tissue contrast distinguishes tumor tissue from normal tissue + Whole-tumor coverage without sample sectioning + Simultaneous imaging of vessels and soft tissue - Long data acquisition times - Resolution is not sufficient to resolve small capillaries; µCT is therefore preferable for pure vascular imaging	40µm
Paper I	SSC-MRI	Voxelwise computation of pre and post contrast R2* in breast xenografts; computation of FBV using equation (1.11)	FBV values were overestimated by SSC-MRI compared to µCT, but the distribution of FBV was similar for both modalities. SSC-MRI was able to visualize higher FBV in tumor rim compared to tumor center.	+ In addition to FBV, computation of vessel size and density possible - Model-based computation of absolute FBV requires knowledge of $\Delta\chi$	0.1mm
Paper II & III	DCE-MRI	In paper II, vascular function was assessed using RSI, AUC, FEV and parameters based on the Tofts-model (K^{trans}, v_e, v_p). In paper III, DCE-MRI was used to visualize the kinetics of nanoemulsions containing Gd contrast agent.	In paper II, RSI, AUC, FEV and v_e rose significantly in both BEZ235-treated ovarian tumor xenograft models compared to the control xenografts. In paper III, DCE-MRI visualized accumulation of RGD targeted nanoemulsion mainly in the tumor rim while the control nanoemulsion reached the central tumor to a larger extend. In the tumor rim, the targeted nanoemulsion accumulated faster than the control nanoemulsion and showed a periodicity in the accumulation, which may be attributed to receptor binding and recycling kinetics.	+ *In vivo* imaging modality + Repeated measurements possible + Can be used in humans + Can be combined e.g. with anatomical imaging +/- Sensitive to perfused blood vessels only	0.36 mm
				+ Assessment of vascular function -Parameters are not easily interpretable, e.g. K^{trans} depends both on vessel permeability and perfusion - Vascular parameters K^{trans}, v_e and v_p are based on tracer-kinetic models - VIF required for computation of model-based parameters; acquisition of a suitable VIF can be challenging	0.45mm
					mm

5.2.1 Imaging of vascular morphology

In paper I, three imaging modalities were compared in their ability to visualize tumor vascularization and measure tumor FBV. Of these modalities, **µCT** can be regarded as the best modality to directly portray the tumor vasculature. In subsequent papers, µCT of breast tumors was also used to characterize the vascular differences in tumors grown for 3 vs. 5 weeks [121] and to simulate tumor blood flow using bioimage informatics approaches [126]. In these studies, µCT was regarded as the 'gold standard' although the resolution of 8 µm was not sufficient to visualize the smallest capillaries. Still, other studies use even lower resolutions to study tumor vascularization [103] and vascular response to treatment [102]. In another recent study that also used Microfil as a contrast agent, µCT was performed at resolutions down to 3.4 µm and vessel diameters correlated excellently with histology [127]. With improvements in µCT scanner hardware, µCT at such high resolution will probably be more widely used in studies of angiogenesis.

In paper I, **µMRI** was also used to image the tumor vasculature *ex vivo*. While this method has the advantage that the soft tissue contrast can provide useful complementary data, it lacks the high resolution of µCT, which resulted in an overestimation of the FBV due to partial volume effects. In addition, µMRI at high resolution is very time consuming, which makes this method suboptimal for the sole purpose of imaging tumor vasculature. While µMRI is inferior to µCT with regard to vascular imaging, it has helped in paper II to distinguish tumor vessels from peritumoral vessels (**Fig. 10**).

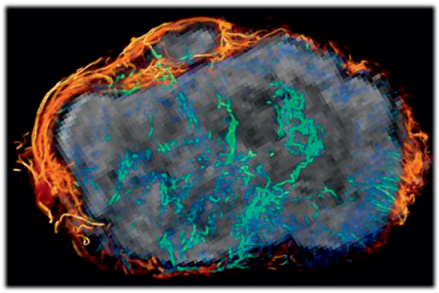

Figure 10: High resolution µMRI data (grey) overlaid with µCT derived vasculature. The tumor vasculature is color coded in green/blue and the peritumoral vasculature in orange.

As already explained in chapter 5.1.1, **SSC-MRI** was compared to the µCT data, and it was shown that the FBV distributions were similar. While SSC-MRI is not routinely

used in the clinic, it has been used in clinical trials. To mention a few applications, FBV has been shown to correlate with tumor grade in human gliomas [128,129] and vessel size has been shown to decrease in gliomas as early as one day after treatment with cediranib [130].

Overall, the results in this thesis in comparison with other studies suggest that μCT is an excellent and unique method for visualizing the 3D tumor vasculature *ex vivo*, while SSC-MRI is a promising method for studying vascular morphology *in vivo*.

5.2.2 Imaging of *in vivo* nanoparticle distribution in tumors using DCE-MRI and IVM

There is an increasing amount of research being performed for the development of nanoparticles that can be used for targeted delivery of cancer therapeutics and for cancer diagnostic purposes. Such nanoparticles often contain contrast agents to facilitate the observation of their distribution *in vivo*. Appropriate contrast agents permit the visualization of nanoparticles e.g. using fluorescent imaging with IVM [117], whole body or tumor near infrared fluorescent imaging [131,132], nuclear imaging [133], CT [134] or MRI [135]. Among these imaging modalities, MRI has the advantages of providing whole tumor coverage and simultaneous anatomical imaging. Conventionally, MRI has been used to assess relative nanoparticle concentration in the tissue at set time points after administration. In the case of targeted nanoparticles, this helps to assess the relative concentration and distribution of the target sites. However, quantification of nanoparticle accumulation rates or targeting kinetics require repeated imaging with a temporal resolution suitable for description of ligand binding kinetics [117].

In paper III, an interesting multi-modality approach for studying nanoparticle kinetics was developed and its potential use to study vascular endothelial cell receptor dynamics was demonstrated. The multi-functional nanoemulsion, RGD-targeted or non-targeted control, was previously characterized and strong indications of cellular uptake of the RGD-targeted nanoemulsion were found [117]. In paper III, DCE-MRI revealed differences in accumulation rates for targeted and control nanoemulsion, i.e. the targeted nanoemulsion accumulated rapidly in the tumor rim, while the control nanoemulsion

accumulated more evenly throughout the tumor. The faster accumulation of the targeted nanoemulsion was observed previously by IVM [117], and the preferential targeting in the tumor rim has also been detected before and may be caused by the higher angiogenic activity in the tumor rim [132]. The MR images were acquired at a spatial resolution of 0.45 × 0.45 × 1 mm^3 and a temporal resolution of 21.6 s. This relatively high temporal resolution permitted the quantification of the nanoemulsion targeting rates. With population-based VIFs, which were acquired by IVM for targeted and control nanoemulsion, the signal enhancement curves from the tumor rim were analyzed using the extended Tofts model. The estimated parameter K_i was about 10 times higher for the RGD nanoemulsion and v_e was smaller, which again suggests that the RGD nanoemulsion accumulated faster and, additionally, more closely to the vasculature without diffusing far into the EES.

Interestingly, the high temporal resolution permitted the observation of a periodicity in the enhancement curve of the targeted nanoemulsion. It was hypothesized that this periodicity originates from the receptor binding-internalization-recycling kinetics, which seems plausible as the period of the curve was in accordance with the range of the recycling half-lives of $\alpha_v\beta_3$ integrin [28]. In a study by Oostendorp et al., Gd-containing nanoparticles were targeted to the CD13 receptor on endothelial cells, and the enhancement curves also suggested a periodicity in the accumulation of these targeted nanoparticles [136]. Although this study and our *in vitro* experiments supported the hypothesis that this periodicity is caused by receptor kinetics, the results remain to be reproduced and validated by further experiments.

Though dynamic MRI is not commonly used to assess nanoparticle kinetics in tumors, several other studies have used it to study the kinetics of different targeted nanoparticles. Pharmacokinetic modelling was also used in these studies and showed differences between targeted and control nanoparticles [136-138]. Collectively, dynamic MRI has the potential to become a unique molecular imaging tool for quantification of nanoparticle accumulation rates and estimation of cell receptor expression and receptor dynamics on the whole tumor level. Thereby it may also be used in the design and optimization of nanoparticles and to study drug delivery to tumors.

5.2.3 Imaging of vascular function

In paper II, vascular function was assessed using DCE-MRI, which is a method used both preclinically and clinically. Several parameters, i.e. AUC_{1min}, RSI_{1min} and FEV_{1min} were derived directly from the enhancement curves. while the parameters K^{trans}, v_e and v_p were derived using the Tofts model. K^{trans} is a frequently reported parameter for assessing vascular targeted therapies, but for low-molecular contrast agents such as Omniscan, which is approved for clinical use and was used in study II, this parameter is dependent on capillary permeability, vessel surface area, interstitial fluid pressure and convection, as well as the blood flow in the tissue. Therefore, it is difficult to ascertain the origin of any observed changes in K^{trans}. Interestingly, in paper II, the non-model based parameters found that PI3K/mTor inhibition changed the tumor vasculature significantly, while the model based parameters found no significant changes. The lack of changes in the model based parameters could be attributed violation of model assumptions. One other challenge for quantifying DCE-MRI parameters using model-based approaches is the necessity of a VIF, which should preferably be measured for each patient. However, it has been shown that there can be a high correlation between DCE-MRI parameters computed with individual and population-based VIFs [139]. Therefore, in papers II and III, population based VIFs were used for the data modelling.

Since non-model based parameters are easy to acquire, they should be assessed in trials to determine whether they are more useful for response assessment than model-based parameters. However, these parameters can depend on acquisition details, which should be taken into account when comparing results acquired at different MR systems or using different sequences.

Despite the mentioned drawbacks, DCE-MRI still has advantages over other methods assessing vascular function *in vivo*. DCE-MRI is non-invasive (except for the injection of Gd-containing contrast agents, which in rare cases can cause adverse reactions to Gd), has relatively high resolution, and can easily be combined with other MR imaging sequences.

Other methods for characterizing vascular function are contrast enhanced ultrasound , Doppler ultrasound, DCE-CT or histological analysis following the *in vivo* injection of

dyes that stain perfused vessels or permeate into the EES and can thereby be used to estimate vessel permeability. To describe the advantages and disadvantages of these imaging modalities is beyond the scope of this thesis, but some of these methods are referred to in chapter 5.3.2.

5.3 Multimodal imaging of drug response

The traditional treatment of cancer, besides surgery, are chemotherapy or radiotherapy. When effective, these therapies lead to a reduction in tumor volume, which is usually assessed using MRI or CT or, where applicable, palpation. The newer generation of drugs, such as angiogenesis inhibitors and STIs are often regarded as cytostatic and rather change tumor vasculature, cellularity or cellular metabolism and proliferation before a decrease in tumor volume is measurable [47,82]. In addition, response can be spatially heterogeneous [140].Therefore, better methods are required, that can distinguish between the various forms of treatment response and multi-modal imaging is useful if each modality gives complementary information about the type of response.

In paper II, the PI3K/mTor inhibitor BEZ235 was used to treat mice with ovarian tumor xenografts. Measurement of p-Akt after treatment indicated that xenografts grown from TOV-21G responded strongly to BEZ235, whereas the treatment had minimal impact on signal transduction in xenografts derived from TOV-112D. In the paper, multi-modal MRI was used to assess both the cellular and the vascular response in these two xenograft models.

5.3.1 Cellular response to PI3K/mTor inhibition

PI3K/mTor inhibitors like BEZ235 are STIs that are regarded as cytostatic, and it is frequently suggested that either vascular changes should be measured by DCE-MRI [141,142] or the metabolic response of the tumor cells should be assessed e.g. by FDG-PET [46,143] or hyperpolarized ^{13}C-MRS [144]. Initial testing of BEZ235 did not show that the drug induced apoptosis in cancer cells [33], and DW-MRI has not been mentioned in the literature to be useful for assessing response to PI3K inhibitors. However, recent studies have found that BEZ235 can induce cell death either via

apoptosis [145-147] or autophagy [146,148]. In light of these mentioned studies, the effect of BEZ235 on tumor cells seems to be dependent on the type of cancer cells. In paper II, the effect of this drug on ovarian tumor xenografts was assessed by DW-MRI, and the TOV-21G tumors showed significantly increased ADC values at the post treatment imaging time point (3 days after start of treatment). This increase was of similar magnitude as in studies where ADC increased in patients responding to conventional chemotherapy [149-151] and therefore suggests that DW-MRI may be a suitable method for monitoring treatment response to PI3K/mTor inhibition.

Also, response to other STIs has been explored with DW-MRI, e.g. response to a MEK1/2 inhibitor [152], a Jak1/2 inhibitor [153] and sunitinib [154]; all of these preclinical studies reported an increase in ADC after 3-4 days.

In paper II, decreased tumor volume was observed at the time of DW-MRI acquisition, but ADC can only be a useful biomarker for treatment response if it can measure response earlier than conventional methods, which are based on tumor size measurements. It would therefore be necessary to investigate if changes in ADC are measurable before volumetric changes. Currently, there are no clear guidelines on the usage of DW-MRI for therapy monitoring in cancer. Reproducibility of ADC values needs to be taken into account, and data acquisition parameters, e.g. b-values, need to be standardized. It also still remains to be established how changes in ADC can be used for clinical decision making [155].

Collectively, it can be suggested that DW-MRI should be considered to be incorporated into clinical trials of STIs. In addition, a standardization of ADC measurement and response criteria should be performed so that DW-MRI can be a more useful method for treatment response assessment.

5.3.2 Imaging of changes in vascular function and morphology induced by PI3K inhibition

In paper II, changes in vascular function were assessed with DCE-MRI and changes in morphology with μCT. The challenges regarding the interpretation of DCE-MRI

parameters and some methodological challenges of μCT were discussed in chapter 5.2.3 and chapter 5.1.1, respectively. Here, the focus will be on challenges regarding treatment response, with PI3K targeting as an example.

Anti-angiogenic therapy is associated with changes in tumor vasculature. VEGF-blockers such as bevacizumab directly inhibit angiogenesis, but signal transduction inhibitors such as PI3K inhibitors can also affect angiogenesis [38,156]. In paper II, DCE-MRI was used to assess changes in vascular function and it was found that RSI_{1min}, AUC_{1min} and FEV_{1min} increased significantly in both tumor models upon treatment. Also an increase in K^{trans} was observed. Vascular morphology was assessed by μCT, but no changes were found due to large intra-group variation. These results were compared to results from other studies in which PI3K or PI3K/mTor inhibitors were used. For example, Qayum et al. have investigated the effects of the PI3K/mTor inhibitor PI-103 on the vasculature of SQ20B head and neck carcinomas and FVB-MMT-neu spontaneous mammary carcinomas [157]. While their dose was low enough to not alter tumor growth compared to the control groups, they measured vascular changes in the form of **increased blood flow** using 3D Doppler Ultrasound (US); **increased perfused vascular density**, **increased branch length** and **reduced tortuosity** using i.v. injections of anti-CD31; and **enhanced diffusion** of Hoechst from the vessels into the tumor tissue. Collectively, they interpreted these changes as "vascular normalization". The same authors then investigated the delivery of doxorubicin into the same tumor models after treatment with the specific PI3Kα/δ inhibitor GDC-0941 and found **increased doxorubicin delivery** and, as in the previous study, **increased blood flow** with no effect on tumor growth [158]. Sampath et al. used a PI3K inhibitor (GNE-490) as well as a PI3K/mTor inhibitor (GDC-0980) at doses that slowed down tumor growth [102]. In contrast to the results reported by Qayum et al., Sampath et al. found "antivascular effects" such as **reduced FBV** (referred to as vessel density but equivalent to our definition of FBV) measured by μCT and histology, **increased vessel size** and **decreased vessel density** but **no change in FBV** measured by susceptibility contrast MRI, **decreased blood flow** measured by DCE-US, and **decreased K^{trans}** measured by DCE-MRI. In yet another study, the drug BEZ-235 was used by Schnell et al. in BN472 rat mammary carcinomas [142]. Similar to Sampath et

al., they found inhibited tumor growth and **decreased K^{trans}**. In addition and in contrast to Qayum et al., they found **decreased diffusion** of Evans Blue out of the vessels, suggesting decreased permeability, while there was **no change in vascular density** measured after i.v. Dextran-FITC injection.

By comparing these studies it becomes clear that the vascular response to drugs targeting the PI3K pathway can have various forms as both increases or decreases in various vascular parameters have been measured. The increase in K^{trans} that was measured in paper II therefore suggests that the vascular changes were of a different kind than those measured by Schnell et al. [142] and Sampath et al. [102], which may have been caused by various factors such as cell lines or drug dosage.

The lack of change in vascular morphology in paper II may have been the result of the large intragroup variations. Since µCT is an *ex vivo* imaging method, it is not possible to measure changes in vascular morphology longitudinally in the same mouse. This is clearly a disadvantage over *in vivo* imaging modalities because baseline variations cannot be accounted for.

Surprisingly, in the study by Sampath et al., FBV decrease was measured by µCT but not by SSC-MRI, which indicates that the varying results could also arise when different imaging modalities are used to measure a specific parameter and care should be taken when results are interpreted. Hence, it may be advisable that multi modal imaging is performed routinely in preclinical studies investigating vascular response as in the abovementioned studies.

5.3.3 Cellular versus vascular response

Interestingly, in paper II only the TOV-21G cell line showed a strong cellular response in the form of decreased p-Akt, decreased tumor volume and increased ADC. The TOV-112D xenografts did not show such a cellular response but still exhibited changes in vascular function similar to those seen in the TOV-21G xenografts.

These results indicate that a change in vascular function may not be enough for a tumor to respond to treatment, and in this case, the DCE-MRI parameters may be regarded as

false positive biomarkers. This is an important finding, and it is important to report false positive as well as false negative biomarkers [159] because these biomarkers need to be robust in order to be introduced into clinical practice.

Paper II suggests that ADC may be more sensitive to overall treatment response than DCE-MRI. In addition, DW-MRI has several advantages over DCE-MRI because it is a fast imaging procedure for which no contrast agent administration is required and calculating ADC requires only basic mathematical computations.

In general a combination of DW-MRI and DCE-MRI may be optimal because both cellular and vascular changes can be important for the overall treatment outcome. Still, both DW-MRI and DCE-MRI have similar challenges when it comes to their use for treatment response assessment in clinical applications. Among these are that both methods require more standardized imaging and data analysis procedures [70,82]. In addition, the methods need to become more robust, measurement errors and repeatability of quantitative parameters must be established, and quantitative guidelines for when a change in the imaging biomarkers indicates a treatment response are needed [70,82,143].

6 Conclusions and future perspectives

This thesis demonstrates the wide array of potential applications of multi-modal imaging for preclinical and clinical cancer research. Especially *in vivo* MR imaging has proven to be versatile as it allows assessment of vascular morphology and function as well as other aspects of the tumor microenvironment. It may also be useful for investigating receptor dynamics.

Being able to assess cell receptor dynamics *in vivo* on the whole tumor level may critically advance our understanding of cellular processes, which are usually studied *in vitro* under conditions that do not fully represent the complex tumor environment. We demonstrated that a combination of DCE-MRI and IVM can be used to show differences in accumulation rates of RGD-targeted or non-targeted nanoemulsions. In addition, *in vitro* experiments suggested that the periodicity observed in the accumulation of RGD-targeted nanoemulsions may be caused by receptor internalization and recycling dynamics. These were some of the first experiments leading to these conclusions and in the future, a thorough reproduction of the results and an expansion of the experiments with different cell lines and different receptor targeting is necessary to confirm the results. If the results can be confirmed, this imaging platform may become widely used in the field of molecular imaging.

Imaging of vascular morphology is useful for understanding angiogenic processes and can help with the development of vascular targeting drugs. In this work we have demonstrated that μCT is a powerful method for visualizing tumor vasculature in great detail. The availability of high quality and high resolution vascular structures is important for the field of computational biology. But also for preclinical cancer treatment studies the use of μCT can provide important information on vascular parameters that are conventionally assessed by hot spot analysis in histological data. Since histology does not allow full coverage of tumors, μCT may be considered a superior method in this context. For future studies it would be beneficial if the μCT resolution would be below the smallest vessel size. As the CT-scanners are constantly improving, this is now just a matter of scanner accessibility and costs. Combination of morphological information obtained using μCT with functional information obtained

using MRI would provide a comprehensive multimodal description of tumor vascularity, which would be useful for understanding effects of antiangiogenic drugs in more detail.

For this thesis, three *in vivo* MR imaging modalities were used to characterize tumor xenografts, namely SSC-MRI, DCE-MRI and DW-MRI. For SSC-MRI we demonstrated that the FBV measurements were distributed similarly to those obtained by μCT, but that the values were overestimated. SSC-MRI is not routinely used in the clinic and especially not often outside the brain. The limited availability of approved contrast agents may be a factor preventing it from being used more often. DCE-MRI and DW-MRI were used to assess tumor response to PI3K/mTor inhibition. Importantly, we have demonstrated that DW-MRI may be a suitable method for assessing tumor response to STIs even though these are mostly considered cytostatic. Follow-up studies are required to test if the ADC increase can also be measured before a decrease in tumor volume is measurable, which would be an advantage over conventional assessments of tumor burden. DCE-MRI showed a vascular response in both tumor models, which did not the differential cellular response of the two xenograft models. Therefore, vascular response may not necessarily be sufficient for a complete tumor response.

The multi-modal imaging platforms presented in this thesis provide a fundament for further studies that could be performed to systematically compare imaging biomarkers for response to anti-angiogenic drugs as well as drugs targeting signal transduction pathways. Ultimately, it is desired that guidelines are improved and these biomarkers become so robust that they can aid clinical decision making. The validation of biomarkers reported in this thesis may contribute to a better understanding of how different imaging modalities reflect physiological changes in tumors after therapy. As demonstrated in this work, future therapy monitoring in cancer may depend on combinations of biomarkers rather than single markers. Understanding the individual contributions in multimodal imaging regimens in various contexts will be necessary to bring these methodologies into clinical practice. Progress in this field requires a continued mapping of cellular and vascular responses to treatment and continued development of methods for integration of data from multiple sources.

7 Bibliography

1. World Health Organization. Cancer Fact Sheet N°297. 2014. Available via http://www.who.int/mediacentre/factsheets/fs297/en/ (Accessed 5 Feb 2015)

2. National Cancer Institute. Defining Cancer. 2014. Available via http://www.cancer.gov/cancertopics/cancerlibrary/what-is-cancer (Accessed 15 Nov 2014)

3. Hanahan D, Weinberg RA. The hallmarks of cancer. *Cell* 2000; **100** (1):57-70.

4. Hanahan D, Weinberg RA. Hallmarks of cancer: the next generation. *Cell* 2011; **144** (5):646-674.

5. International Agency for Research on Cancer. Cancer Incidence and Mortality Worldwide: IARC CancerBAse No. 11. 2012. Available via http://globocan.iarc.fr (Accessed 22. Aug 2014)

6. DeSantis CE, Lin CC, Mariotto AB et al. Cancer treatment and survivorship statistics, 2014. *CA Cancer J Clin* 2014; **64** (4):252-271.

7. National Cancer Institute,. SEER Cancer Statistics Review, 1975-2010. 2013. Available via http://seer.cancer.gov/csr/1975_2010 (Accessed 15 Oct 2014)

8. Cancer registry of Norway. Cancer in Norway 2012. 2014. Available via http://www.kreftregisteret.no/Global/Cancer%20in%20Norway/2012/CIN_2012.pdf

9. Siegel R, Naishadham D, Jemal A. Cancer statistics, 2012. *CA Cancer J Clin* 2012; **62** (1):10-29.

10. Vaughan S, Coward JI, Bast RC, Jr. et al. Rethinking ovarian cancer: recommendations for improving outcomes. *Nat Rev Cancer* 2011; **11** (10):719-725.

11. McGuire WP, Hoskins WJ, Brady MF et al. Cyclophosphamide and cisplatin compared with paclitaxel and cisplatin in patients with stage III and stage IV ovarian cancer. *N Engl J Med* 1996; **334** (1):1-6.

12. Banerjee S, Kaye SB. New strategies in the treatment of ovarian cancer: current clinical perspectives and future potential. *Clin Cancer Res* 2013; **19** (5):961-968.

13. Targeted Cancer Therapies. 2014. Available via http://www.cancer.gov/cancertopics/factsheet/Therapy/targeted (Accessed 23.09.2014)

14. Folkman J. Tumor angiogenesis: therapeutic implications. *N Engl J Med* 1971; **285** (21):1182-1186.

15. Folkman J. Role of angiogenesis in tumor growth and metastasis. *Semin Oncol* 2002; **29** (6 Suppl 16):15-18.

16. Carmeliet P, Jain RK. Angiogenesis in cancer and other diseases. *Nature* 2000; **407** (6801):249-257.

17. Semenza G. Signal transduction to hypoxia-inducible factor 1. *Biochem Pharmacol* 2002; **64** (5-6):993-998.

18. Ferrara N. Vascular endothelial growth factor as a target for anticancer therapy. *Oncologist* 2004; **9 Suppl 1**:2-10.

19. Goel S, Duda DG, Xu L et al. Normalization of the vasculature for treatment of cancer and other diseases. *Physiol Rev* 2011; **91** (3):1071-1121.

20. Dvorak HF, Nagy JA, Dvorak JT, Dvorak AM. Identification and characterization of the blood vessels of solid tumors that are leaky to circulating macromolecules. *Am J Pathol* 1988; **133** (1):95-109.

21. Ebos JM, Kerbel RS. Antiangiogenic therapy: impact on invasion, disease progression, and metastasis. *Nat Rev Clin Oncol* 2011; **8** (4):210-221.

22. National Cancer Institute. FDA approval for bevacizumab. 2014. Available via http://www.cancer.gov/cancertopics/druginfo/fda-bevacizumab (Accessed 20 Feb 2015)

23. European Medicines Agency. Avastin. 2014. Available via http://www.ema.europa.eu/ema/index.jsp?curl=pages/medicines/human/medicines/000582/human_med_000663.jsp (Accessed 10 Feb 2015)

24. Bergers G, Hanahan D. Modes of resistance to anti-angiogenic therapy. *Nat Rev Cancer* 2008; **8** (8):592-603.

25. Danhier F, Le Breton A, Preat V. RGD-based strategies to target alpha(v) beta(3) integrin in cancer therapy and diagnosis. *Mol Pharm* 2012; **9** (11):2961-2973.

26. Hynes RO. Integrins: bidirectional, allosteric signaling machines. *Cell* 2002; **110** (6):673-687.

27. Ruoslahti E. RGD and other recognition sequences for integrins. *Annu Rev Cell Dev Biol* 1996; **12**:697-715.

28. Caswell PT, Norman JC. Integrin trafficking and the control of cell migration. *Traffic* 2006; **7** (1):14-21.

29. Stupp R, Hegi ME, Gorlia T et al. Cilengitide combined with standard treatment for patients with newly diagnosed glioblastoma with methylated MGMT promoter (CENTRIC EORTC 26071-22072 study): a multicentre, randomised, open-label, phase 3 trial. *Lancet Oncol* 2014; **15** (10):1100-1108.

30. Schottelius M, Laufer B, Kessler H, Wester HJ. Ligands for mapping alphavbeta3-integrin expression in vivo. *Acc Chem Res* 2009; **42** (7):969-980.

31. Chalhoub N, Baker SJ. PTEN and the PI3-kinase pathway in cancer. *Annu Rev Pathol* 2009; **4**:127-150.

32. Engelman JA, Luo J, Cantley LC. The evolution of phosphatidylinositol 3-kinases as regulators of growth and metabolism. *Nat Rev Genet* 2006; **7** (8):606-619.

33. Maira SM, Stauffer F, Brueggen J et al. Identification and characterization of NVP-BEZ235, a new orally available dual phosphatidylinositol 3-kinase/mammalian target of rapamycin inhibitor with potent in vivo antitumor activity. *Mol Cancer Ther* 2008; **7** (7):1851-1863.

34. Vivanco I, Sawyers CL. The phosphatidylinositol 3-Kinase AKT pathway in human cancer. *Nat Rev Cancer* 2002; **2** (7):489-501.

35. Hemmings BA, Restuccia DF. PI3K-PKB/Akt pathway. *Cold Spring Harb Perspect Biol* 2012; **4** (9):a011189.

36. Zoncu R, Efeyan A, Sabatini DM. mTOR: from growth signal integration to cancer, diabetes and ageing. *Nat Rev Mol Cell Biol* 2011; **12** (1):21-35.

37. Jiang BH, Liu LZ. PI3K/PTEN signaling in angiogenesis and tumorigenesis. *Adv Cancer Res* 2009; **102**:19-65.

38. Karar J, Maity A. PI3K/AKT/mTOR Pathway in Angiogenesis. *Front Mol Neurosci* 2011; **4**:51.

39. Dimmeler S, Fleming I, Fisslthaler B et al. Activation of nitric oxide synthase in endothelial cells by Akt-dependent phosphorylation. *Nature* 1999; **399** (6736):601-605.

40. Sorlie T, Perou CM, Fan C et al. Gene expression profiles do not consistently predict the clinical treatment response in locally advanced breast cancer. *Mol Cancer Ther* 2006; **5** (11):2914-2918.

41. Eisenhauer EA, Therasse P, Bogaerts J et al. New response evaluation criteria in solid tumours: revised RECIST guideline (version 1.1). *Eur J Cancer* 2009; **45** (2):228-247.

42. Schroder FH, Hugosson J, Roobol MJ et al. Screening and prostate-cancer mortality in a randomized European study. *N Engl J Med* 2009; **360** (13):1320-1328.

43. Rustin GJ, Vergote I, Eisenhauer E et al. Definitions for response and progression in ovarian cancer clinical trials incorporating RECIST 1.1 and CA 125 agreed by the Gynecological Cancer Intergroup (GCIG). *Int J Gynecol Cancer* 2011; **21** (2):419-423.

44. Wallace TJ, Torre T, Grob M et al. Current approaches, challenges and future directions for monitoring treatment response in prostate cancer. *J Cancer* 2014; **5** (1):3-24.

45. Ferrandina G, Ludovisi M, Corrado G et al. Prognostic role of Ca125 response criteria and RECIST criteria: analysis of results from the MITO-3 phase III trial of gemcitabine versus pegylated liposomal doxorubicin in recurrent ovarian cancer. *Gynecol Oncol* 2008; **109** (2):187-193.

46. Tunariu N, Kaye SB, Desouza NM. Functional imaging: what evidence is there for its utility in clinical trials of targeted therapies? *Br J Cancer* 2012; **106** (4):619-628.

47. Serkova NJ. Translational imaging endpoints to predict treatment response to novel targeted anticancer agents. *Drug Resist Updat* 2011; **14** (4-5):224-235.

48. Desar IM, van Herpen CM, van Laarhoven HW et al. Beyond RECIST: molecular and functional imaging techniques for evaluation of response to targeted therapy. *Cancer Treat Rev* 2009; **35** (4):309-321.

49. Jain RK. Transport of molecules in the tumor interstitium: a review. *Cancer Res* 1987; **47** (12):3039-3051.

50. Hatzis C, Bedard PL, Birkbak NJ et al. Enhancing Reproducibility in Cancer Drug Screening: How Do We Move Forward? *Cancer Res* 2014; **74** (15):4016-4023.

51. Workman P, Aboagye EO, Balkwill F et al. Guidelines for the welfare and use of animals in cancer research. *Br J Cancer* 2010; **102** (11):1555-1577.

52. Cespedes MV, Casanova I, Parreno M, Mangues R. Mouse models in oncogenesis and cancer therapy. *Clin Transl Oncol* 2006; **8** (5):318-329.

53. Eklund L, Bry M, Alitalo K. Mouse models for studying angiogenesis and lymphangiogenesis in cancer. *Mol Oncol* 2013; **7** (2):259-282.

54. Johnson JI, Decker S, Zaharevitz D et al. Relationships between drug activity in NCI preclinical in vitro and in vivo models and early clinical trials. *Br J Cancer* 2001; **84** (10):1424-1431.

55. Kerbel RS. Human tumor xenografts as predictive preclinical models for anticancer drug activity in humans: better than commonly perceived-but they can be improved. *Cancer Biol Ther* 2003; **2** (4 Suppl 1):S134-139.

56. Fass L. Imaging and cancer: a review. *Mol Oncol* 2008; **2** (2):115-152.

57. Rabi II, Zacharias JR, Millman S, Kusch P. A New Method of Measuring Nuclear Magnetic Moment. *Physical Review* 1938; **53** (4):318-318.

58. Bloch F. Nuclear Induction. *Physical Review* 1946; **70** (7-8):460-474.

59. Purcell EM, Torrey HC, Pound RV. Resonance Absorption by Nuclear Magnetic Moments in a Solid. *Physical Review* 1946; **69** (1-2):37-38.

60. Paul L. MRI - a new way of seeing. *Nature* 1973; **242**:190-191.

61. Mansfield P, Grannell PK. NMR 'diffraction' in solids? *Journal of Physics C: Solid State Physics* 1973; **6** (22):L422.

62. Levitt MH (2008) Spin Dynamics: Basics of Nuclear Magnetic Resonance.

63. Brown R.W. CYN, Haacke E.M., Thompson M.R., Venkatesan R. (2014) Magnetic Resonance Imaging Physical Principles and Sequence Design.

64. Bloembergen N, Purcell EM, Pound RV. Relaxation Effects in Nuclear Magnetic Resonance Absorption. *Physical Review* 1948; **73** (7):679-712.

65. Koenig SH, Brown RD, 3rd. Relaxation of solvent protons by paramagnetic ions and its dependence on magnetic field and chemical environment: implications for NMR imaging. *Magn Reson Med* 1984; **1** (4):478-495.

66. Gowland P, Mansfield P, Bullock P et al. Dynamic studies of gadolinium uptake in brain tumors using inversion-recovery echo-planar imaging. *Magn Reson Med* 1992; **26** (2):241-258.

67. Strijkers GJ, Mulder WJ, van Tilborg GA, Nicolay K. MRI contrast agents: current status and future perspectives. *Anticancer Agents Med Chem* 2007; **7** (3):291-305.

68. Rohrer M, Bauer H, Mintorovitch J et al. Comparison of magnetic properties of MRI contrast media solutions at different magnetic field strengths. *Invest Radiol* 2005; **40** (11):715-724.

69. Stejskal EO, Tanner JE. Spin Diffusion Measurements: Spin Echoes in the Presence of a Time-Dependent Field Gradient. *The Journal of Chemical Physics* 1965; **42** (1):288-292.

70. Padhani AR, Liu G, Koh DM et al. Diffusion-weighted magnetic resonance imaging as a cancer biomarker: consensus and recommendations. *Neoplasia* 2009; **11** (2):102-125.

71. Gibbs P, Liney GP, Pickles MD et al. Correlation of ADC and T2 measurements with cell density in prostate cancer at 3.0 Tesla. *Invest Radiol* 2009; **44** (9):572-576.

72. Humphries PD, Sebire NJ, Siegel MJ, Olsen OE. Tumors in pediatric patients at diffusion-weighted MR imaging: apparent diffusion coefficient and tumor cellularity. *Radiology* 2007; **245** (3):848-854.

73. Lyng H, Haraldseth O, Rofstad EK. Measurement of cell density and necrotic fraction in human melanoma xenografts by diffusion weighted magnetic resonance imaging. *Magn Reson Med* 2000; **43** (6):828-836.

74. Hamstra DA, Rehemtulla A, Ross BD. Diffusion magnetic resonance imaging: a biomarker for treatment response in oncology. *J Clin Oncol* 2007; **25** (26):4104-4109.

75. Eichler AF, Batchelor TT, Henson JW. Diffusion and perfusion imaging in subacute neurotoxicity following high-dose intravenous methotrexate. *Neuro Oncol* 2007; **9** (3):373-377.

76. Tofts PS, Brix G, Buckley DL et al. Estimating kinetic parameters from dynamic contrast-enhanced T(1)-weighted MRI of a diffusable tracer: standardized quantities and symbols. *J Magn Reson Imaging* 1999; **10** (3):223-232.

77. Tofts PS. Modeling tracer kinetics in dynamic Gd-DTPA MR imaging. *J Magn Reson Imaging* 1997; **7** (1):91-101.

78. Larsson HB, Courivaud F, Rostrup E, Hansen AE. Measurement of brain perfusion, blood volume, and blood-brain barrier permeability, using dynamic contrast-enhanced T(1)-weighted MRI at 3 tesla. *Magn Reson Med* 2009; **62** (5):1270-1281.

79. Jensen LR, Berge K, Bathen TF et al. Effect of dietary tetradecylthioacetic acid on colon cancer growth studied by dynamic contrast enhanced MRI. *Cancer Biol Ther* 2007; **6** (11):1810-1816.

80. Parker GJ, Roberts C, Macdonald A et al. Experimentally-derived functional form for a population-averaged high-temporal-resolution arterial input function for dynamic contrast-enhanced MRI. *Magn Reson Med* 2006; **56** (5):993-1000.

81. Larsson HBW, Stubgaard M, Frederiksen JL et al. Quantitation of blood-brain barrier defect by magnetic resonance imaging and gadolinium-DTPA in patients with multiple sclerosis and brain tumors. *Magnetic Resonance in Medicine* 1990; **16** (1):117-131.

82. Leach MO, Brindle KM, Evelhoch JL et al. The assessment of antiangiogenic and antivascular therapies in early-stage clinical trials using magnetic resonance imaging: issues and recommendations. *Br J Cancer* 2005; **92** (9):1599-1610.

83. O'Connor JP, Jackson A, Parker GJ et al. Dynamic contrast-enhanced MRI in clinical trials of antivascular therapies. *Nat Rev Clin Oncol* 2012; **9** (3):167-177.

84. Boxerman JL, Hamberg LM, Rosen BR, Weisskoff RM. MR contrast due to intravascular magnetic susceptibility perturbations. *Magn Reson Med* 1995; **34** (4):555-566.

85. Tropres I, Grimault S, Vaeth A et al. Vessel size imaging. *Magn Reson Med* 2001; **45** (3):397-408.

86. Dennie J, Mandeville JB, Boxerman JL et al. NMR imaging of changes in vascular morphology due to tumor angiogenesis. *Magn Reson Med* 1998; **40** (6):793-799.

87. Jensen JH, Chandra R. MR imaging of microvasculature. *Magn Reson Med* 2000; **44** (2):224-230.

88. Christen T, Ni W, Qiu D et al. High-resolution cerebral blood volume imaging in humans using the blood pool contrast agent ferumoxytol. *Magn Reson Med* 2012.

89. Fredrickson J SN, Carano R, Wyatt S, Pirzkall A, Weekes C, Silverman J, Rosen L, de Crespigny A Clinical translation of VSI using Ferumoxytol: Feasibility in a phase I oncology clinical trial population. In: 20th Scientific Meeting of the International Society of Magnetic Resonance in Medicine, Melbourne, Australia, 2012.

90. Cormack AM. Reconstruction of densities from their projections, with applications in radiological physics. *Phys Med Biol* 1973; **18** (2):195-207.

91. Hounsfield GN. Computerized transverse axial scanning (tomography). 1. Description of system. *Br J Radiol* 1973; **46** (552):1016-1022.

92. Hsieh J (2003) Computed Tomography - Principles, Design, Artifacts and Recent Advances. SPIE- The International Society for Optical Engineering, Bellingham, WA

93. Zagorchev L, Oses P, Zhuang ZW et al. Micro computed tomography for vascular exploration. *J Angiogenes Res*; **2**:7.

94. Ritman EL. Micro-computed tomography-current status and developments. *Annu Rev Biomed Eng* 2004; **6**:185-208.

95. Schambach SJ, Bag S, Schilling L et al. Application of micro-CT in small animal imaging. *Methods* 2010; **50** (1):2-13.

96. Ritman EL. Current status of developments and applications of micro-CT. *Annu Rev Biomed Eng* 2011; **13**:531-552.

97. Clark DP, Badea CT. Micro-CT of rodents: State-of-the-art and future perspectives. *Phys Med* 2014; **30** (6):619-634.

98. Müller BL, L; Dominietto, M; Rudin, M; Schulz, G; Deyhle, H; Germann, M; Pfeiffer, Franz; David, C; Weitkamp, T High-resolution tomographic imaging of microvessels. In: Proc. of SPIE, 2008.

99. Williamson MJ, Silva MD, Terkelsen J et al. The relationship among tumor architecture, pharmacokinetics, pharmacodynamics, and efficacy of bortezomib in mouse xenograft models. *Mol Cancer Ther* 2009; **8** (12):3234-3243.

100. Savai R, Langheinrich AC, Schermuly RT et al. Evaluation of angiogenesis using micro-computed tomography in a xenograft mouse model of lung cancer. *Neoplasia* 2009; **11** (1):48-56.

101. Shojaei F, Wu X, Zhong C et al. Bv8 regulates myeloid-cell-dependent tumour angiogenesis. *Nature* 2007; **450** (7171):825-831.

102. Sampath D, Oeh J, Wyatt SK et al. Multimodal Microvascular Imaging Reveals that Selective Inhibition of Class I PI3K Is Sufficient to Induce an Antivascular Response. *Neoplasia* 2013; **15** (7):694-711.

103. Ungersma SE, Pacheco G, Ho C et al. Vessel imaging with viable tumor analysis for quantification of tumor angiogenesis. *Magn Reson Med* 2010; **63** (6):1637-1647.

104. Jain RK, Schlenger K, Hockel M, Yuan F. Quantitative angiogenesis assays: progress and problems. *Nat Med* 1997; **3** (11):1203-1208.

105. Koehl GE, Gaumann A, Geissler EK. Intravital microscopy of tumor angiogenesis and regression in the dorsal skin fold chamber: mechanistic insights and preclinical testing of therapeutic strategies. *Clin Exp Metastasis* 2009; **26** (4):329-344.

106. Hak S, Reitan NK, Haraldseth O, de Lange Davies C. Intravital microscopy in window chambers: a unique tool to study tumor angiogenesis and delivery of nanoparticles. *Angiogenesis* 2010; **13** (2):113-130.

107. Jain RK, Munn LL, Fukumura D. Dissecting tumour pathophysiology using intravital microscopy. *Nat Rev Cancer* 2002; **2** (4):266-276.

108. Monsky WL, Mouta Carreira C, Tsuzuki Y et al. Role of host microenvironment in angiogenesis and microvascular functions in human breast cancer xenografts: mammary fat pad versus cranial tumors. *Clin Cancer Res* 2002; **8** (4):1008-1013.

109. Rege A, Thakor NV, Pathak AP. Optical Imaging of Microvascular Morphology and Perfusion. *Curr Angiogenesis* 2012; **1** (3):243-260.

110. Lawrence MJ, Rees GD. Microemulsion-based media as novel drug delivery systems. *Adv Drug Deliv Rev* 2000; **45** (1):89-121.

111. Mulder WJ, Strijkers GJ, van Tilborg GA et al. Lipid-based nanoparticles for contrast-enhanced MRI and molecular imaging. *NMR Biomed* 2006; **19** (1):142-164.

112. Maruyama K. Intracellular targeting delivery of liposomal drugs to solid tumors based on EPR effects. *Adv Drug Deliv Rev* 2011; **63** (3):161-169.

113. Brinkley BR, Beall PT, Wible LJ et al. Variations in cell form and cytoskeleton in human breast carcinoma cells in vitro. *Cancer Res* 1980; **40** (9):3118-3129.

114. Lacroix M, Leclercq G. Relevance of breast cancer cell lines as models for breast tumours: an update. *Breast Cancer Res Treat* 2004; **83** (3):249-289.

115. Bhujwalla ZM, Artemov D, Natarajan K et al. Vascular differences detected by MRI for metastatic versus nonmetastatic breast and prostate cancer xenografts. *Neoplasia* 2001; **3** (2):143-153.

116. Provencher DM, Lounis H, Champoux L et al. Characterization of four novel epithelial ovarian cancer cell lines. *In Vitro Cell Dev Biol Anim* 2000; **36** (6):357-361.

117. Hak S, Helgesen E, Hektoen HH et al. The effect of nanoparticle polyethylene glycol surface density on ligand-directed tumor targeting studied in vivo by dual modality imaging. *ACS Nano* 2012; **6** (6):5648-5658.

118. Scholzen T, Gerdes J. The Ki-67 protein: from the known and the unknown. *J Cell Physiol* 2000; **182** (3):311-322.

119. Jackson DE. The unfolding tale of PECAM-1. *FEBS Lett* 2003; **540** (1-3):7-14.

120. Kapuscinski J. DAPI: a DNA-specific fluorescent probe. *Biotech Histochem* 1995; **70** (5):220-233.

121. Kim E, Cebulla J, Douglas Ward B et al. Assessing breast cancer angiogenesis in vivo: Which susceptibility contrast MRI biomarkers are relevant? *Magn Reson Med* 2012.

122. Burrell JS, Bradley RS, Walker-Samuel S et al. MRI measurements of vessel calibre in tumour xenografts: comparison with vascular corrosion casting. *Microvasc Res* 2012; **84** (3):323-329.

123. Sundquist T MR, Niles A, O'Brien M, Riss T. Timing your apoptosis assays. *Cell Notes* 2006; (16).

124. Kim SH, Cha ES, Kim HS et al. Diffusion-weighted imaging of breast cancer: correlation of the apparent diffusion coefficient value with prognostic factors. *J Magn Reson Imaging* 2009; **30** (3):615-620.

125. Onishi N, Kanao S, Kataoka M et al. Apparent diffusion coefficient as a potential surrogate marker for Ki-67 index in mucinous breast carcinoma. *J Magn Reson Imaging* 2014.

126. Stamatelos SK, Kim E, Pathak AP, Popel AS. A bioimage informatics based reconstruction of breast tumor microvasculature with computational blood flow predictions. *Microvasc Res* 2014; **91**:8-21.

127. Ehling J, Theek B, Gremse F et al. Micro-CT imaging of tumor angiogenesis: quantitative measures describing micromorphology and vascularization. *Am J Pathol* 2014; **184** (2):431-441.

128. Shin JH, Lee HK, Kwun BD et al. Using relative cerebral blood flow and volume to evaluate the histopathologic grade of cerebral gliomas: preliminary results. *AJR Am J Roentgenol* 2002; **179** (3):783-789.

129. Boxerman JL, Schmainda KM, Weisskoff RM. Relative cerebral blood volume maps corrected for contrast agent extravasation significantly correlate with glioma tumor grade, whereas uncorrected maps do not. *AJNR Am J Neuroradiol* 2006; **27** (4):859-867.

130. Emblem KE, Mouridsen K, Bjornerud A et al. Vessel architectural imaging identifies cancer patient responders to anti-angiogenic therapy. *Nat Med* 2013; **19** (9):1178-1183.

131. Eggen S, Afadzi M, Nilssen EA et al. Ultrasound improves the uptake and distribution of liposomal Doxorubicin in prostate cancer xenografts. *Ultrasound Med Biol* 2013; **39** (7):1255-1266.

132. Jarzyna PA, Deddens LH, Kann BH et al. Tumor angiogenesis phenotyping by nanoparticle-facilitated magnetic resonance and near-infrared fluorescence molecular imaging. *Neoplasia* 2012; **14** (10):964-973.

133. Mitra A, Nan A, Line BR, Ghandehari H. Nanocarriers for nuclear imaging and radiotherapy of cancer. *Curr Pharm Des* 2006; **12** (36):4729-4749.

134. Cormode DP, Skajaa T, van Schooneveld MM et al. Nanocrystal core high-density lipoproteins: a multimodality contrast agent platform. *Nano Lett* 2008; **8** (11):3715-3723.

135. Sipkins DA, Cheresh DA, Kazemi MR et al. Detection of tumor angiogenesis in vivo by alphaVbeta3-targeted magnetic resonance imaging. *Nat Med* 1998; **4** (5):623-626.

136. Oostendorp M, Douma K, Hackeng TM et al. Pharmacokinetics of contrast agents targeted to the tumor vasculature in molecular magnetic resonance imaging. *Contrast Media Mol Imaging* 2010; **5** (1):9-17.

137. Kessinger CW, Togao O, Khemtong C et al. Investigation of In Vivo Targeting Kinetics of alpha(v)beta(3)-Specific Superparamagnetic Nanoprobes by Time-Resolved MRI. *Theranostics* 2011; **1**:263-273.

138. Neubauer AM, Sim H, Winter PM et al. Nanoparticle pharmacokinetic profiling in vivo using magnetic resonance imaging. *Magn Reson Med* 2008; **60** (6):1353-1361.

139. Loveless ME, Halliday J, Liess C et al. A quantitative comparison of the influence of individual versus population-derived vascular input functions on dynamic contrast enhanced-MRI in small animals. *Magn Reson Med* 2012; **67** (1):226-236.

140. O'Connor JP, Rose CJ, Waterton JC et al. Imaging Intratumor Heterogeneity: Role in Therapy Response, Resistance, and Clinical Outcome. *Clin Cancer Res* 2015; **21** (2):249-257.

141. Maira SM, Stauffer F, Schnell C, Garcia-Echeverria C. PI3K inhibitors for cancer treatment: where do we stand? *Biochem Soc Trans* 2009; **37** (Pt 1):265-272.

142. Schnell CR, Stauffer F, Allegrini PR et al. Effects of the dual phosphatidylinositol 3-kinase/mammalian target of rapamycin inhibitor NVP-BEZ235 on the tumor vasculature: implications for clinical imaging. *Cancer Res* 2008; **68** (16):6598-6607.

143. Figueiras RG, Padhani AR, Goh VJ et al. Novel oncologic drugs: what they do and how they affect images. *Radiographics* 2011; **31** (7):2059-2091.

144. Ward CS, Venkatesh HS, Chaumeil MM et al. Noninvasive detection of target modulation following phosphatidylinositol 3-kinase inhibition using hyperpolarized 13C magnetic resonance spectroscopy. *Cancer Res* 2010; **70** (4):1296-1305.

145. Santiskulvong C, Konecny GE, Fekete M et al. Dual targeting of phosphoinositide 3-kinase and mammalian target of rapamycin using NVP-BEZ235 as a novel therapeutic approach in human ovarian carcinoma. *Clin Cancer Res* 2011; **17** (8):2373-2384.

146. Hong SW, Shin JS, Moon JH et al. NVP-BEZ235, a dual PI3K/mTOR inhibitor, induces cell death through alternate routes in prostate cancer cells depending on the PTEN genotype. *Apoptosis* 2014; **19** (5):895-904.

147. Brachmann SM, Hofmann I, Schnell C et al. Specific apoptosis induction by the dual PI3K/mTor inhibitor NVP-BEZ235 in HER2 amplified and PIK3CA mutant breast cancer cells. *Proc Natl Acad Sci U S A* 2009; **106** (52):22299-22304.

148. Liu TJ, Koul D, LaFortune T et al. NVP-BEZ235, a novel dual phosphatidylinositol 3-kinase/mammalian target of rapamycin inhibitor, elicits multifaceted antitumor activities in human gliomas. *Mol Cancer Ther* 2009; **8** (8):2204-2210.

149. Kyriazi S, Collins DJ, Messiou C et al. Metastatic ovarian and primary peritoneal cancer: assessing chemotherapy response with diffusion-weighted MR imaging--value of histogram analysis of apparent diffusion coefficients. *Radiology* 2011; **261** (1):182-192.

150. Cui Y, Zhang XP, Sun YS et al. Apparent diffusion coefficient: potential imaging biomarker for prediction and early detection of response to chemotherapy in hepatic metastases. *Radiology* 2008; **248** (3):894-900.

151. Li XR, Cheng LQ, Liu M et al. DW-MRI ADC values can predict treatment response in patients with locally advanced breast cancer undergoing neoadjuvant chemotherapy. *Med Oncol* 2012; **29** (2):425-431.

152. Beloueche-Babari M, Jamin Y, Arunan V et al. Acute tumour response to the MEK1/2 inhibitor selumetinib (AZD6244, ARRY-142886) evaluated by non-invasive diffusion-weighted MRI. *Br J Cancer* 2013; **109** (6):1562-1569.

153. Loveless ME, Lawson D, Collins M et al. Comparisons of the efficacy of a Jak1/2 inhibitor (AZD1480) with a VEGF signaling inhibitor (cediranib) and sham treatments in mouse tumors using DCE-MRI, DW-MRI, and histology. *Neoplasia* 2012; **14** (1):54-64.

154. Gaustad JV, Pozdniakova V, Hompland T et al. Magnetic resonance imaging identifies early effects of sunitinib treatment in human melanoma xenografts. *J Exp Clin Cancer Res* 2013; **32**:93.

155. Li SP, Padhani AR. Tumor response assessments with diffusion and perfusion MRI. *J Magn Reson Imaging* 2012; **35** (4):745-763.

156. Brader S, Eccles SA. Phosphoinositide 3-kinase signalling pathways in tumor progression, invasion and angiogenesis. *Tumori* 2004; **90** (1):2-8.

157. Qayum N, Muschel RJ, Im JH et al. Tumor vascular changes mediated by inhibition of oncogenic signaling. *Cancer Res* 2009; **69** (15):6347-6354.

158. Qayum N, Im J, Stratford MR et al. Modulation of the tumor microvasculature by phosphoinositide-3 kinase inhibition increases doxorubicin delivery in vivo. *Clin Cancer Res* 2012; **18** (1):161-169.

159. Boult JK, Jamin Y, Jacobs V et al. False-negative MRI biomarkers of tumour response to targeted cancer therapeutics. *Br J Cancer* 2012; **106** (12):1960-1966.

Paper I

Is not included due to copyright

Paper II

Is not included due to copyright

Paper III

Is not included due to copyright